Calibration Methods of an Acoustic Doppler Current Profiler & Investigations of the Critical Wavenumber in Unstable Evaporating Thin Films

By

Eric W. Kalenauskas

A THESIS

Submitted in partial fulfillment of the requirements

for the degree of

Master of Science in Mechanical Engineering

MICHIGAN TECHNOLOGICAL UNIVERSITY

2009

This thesis, "Calibration Methods of an Acoustic Doppler Current Profiler & Investigations of the Critical Wavenumber in Unstable Evaporating Thin Films" is hereby approved in partial fulfillment of the requirements of the Degree of Master of Science in Mechanical Engineering.

Department of Mechanical Engineering - Engineering Mechanics

Advisor: ______________________________
Dr. Jeffrey S. Allen

Committee Member: ______________________________
Dr. Robert Kolkka

Committee Member: ______________________________
Dr. Gordon Parker

Department Chair: ______________________________
Professor William W. Predebon

Date: ______________________________

ABSTRACT

The following thesis covers the two main research projects the author participated in for the completion of the MS Mechanical Engineering degree. Chapter 1 covers the analysis performed in support of calibrating an acoustic doppler current profiler. Chapter 2 discusses Schlieren photographs of evaporating thin liquid films and the trends of the observable physical wavelengths of the instabilities in the images. Chapter three provides an overview of efforts made in extracting wavelengths in the images automatically. Finally, chapter 4 discusses the behavior of the critical wavenumber in a one-sided evaporation model and corrects and assumption used in related work.

ACKNOWLEDGMENTS

I would like to acknowledge and extend a hearty thanks to Dr. Jeffrey Allen, Dr. Mohan Rao, Dr. Robert Kolkka, Robert Rowe and all the other faculty and staff, in and out of the department, who lent their guidance, encouragement and, not least of all, time in helping with these projects. I would also like to thank my family and my wonderful fiancée for all of their support and encouragement.

CONTENTS

LIST OF FIGURES

LIST OF TABLES

1. CALIBRATION OF AN ACOUSITC DOPPLER CURRENT PROFILER

1.1 ADCP Project Overview

This project was in support of South Florida Water Management District's (SFWMD) use of Acoustic Doppler Current Profilers (ADCPs) to monitor and control the flow of water from Lake Okeechobee through the Everglades and eventually to the Atlantic Ocean. Flow control is important to provide irrigation to the vibrant agricultural areas of south Florida and also to mitigate flooding from hurricanes and heavy rain and also drought. The ADCP is one of the main monitoring devices used by SFWMD however the error associated with the device is not known. The purpose of this project is to determine the bias and uncertainty of measurements taken with an ADCP.

An ADCP is a device used to gather bathymetric data in oceans, lakes and rivers. To obtain a velocity profile, a series of ultrasonic pulses are emitted from its four sensor faces and the resulting signal reflections are recorded by the instrument. The time of the pulse between emitting and recording determines the depth of the measurement and the change in pulse frequency determines the water velocity based on the Doppler effect. The four sensors allow for three dimensional imaging and a verification by the fourth sensor.

This project is a joint senior design/graduate research project. The main task of the senior design team is to design and implement a calibration system for the ADCP. The graduate portion of the project is to analyze the data gathered by the senior design team. A very detailed discussion of the design and implementation of the testing systems can be found in the senior design team's report. [4] The work presented here is the graduate portion of the project involving the data analysis.

A data set from the ADCP consists of velocity measurements in two spatial dimensions: depth and position along the ADCP's scan of the water body of interest. Collectively, this data set is referred to as a transect. The velocities are reported at each depth along the transect in bins to form a velocity profile cross section.

The testing strategy is to provide the ADCP with a controlled and known flow where the velocity is uniform. This should result in a uniform distribution of velocity bins in the transect. The differences between data bins to the mean flow are then analyzed. Two different systems were used for the testing. The first involved a boat that would push a large, open ended tube through water on a lake. The second method involved towing a raft in a small pond at a constant velocity. Both methods assume still water such that all of the velocity is due to the motion of the testing vessel.

1.2 Analysis Method for ADCP Reported Results

The data from both the timed velocities of the raft and ADCP measured velocities are statistically analyzed to determine the validity of the reference measurement and the bias and variability of the ADCP. These results are discussed and compared to similar past works. The results of the open tunnel testing performed on the pontoon boat are also presented and discussed.

The velocity in each bin is actually sampled hundreds of times by the ADCP, the result of which is averaged and reported. The ADCP acquires and reports the transect data through a software program called WinRiver™that is designed specifically for use with the ADCP. The way the ADCP and WinRiver™software condition and process the signals is beyond the scope of this investigation. As such, the ADCP / WinRiver™software system is considered as a "black box" to be calibrated with known a velocity flow in and reported velocity bins out.

The velocity magnitudes for each bin as reported in the WinRiver™results file are collected into an Excel™file for each run. Bad bins are not considered. Bad bins are generated when the ADCP can not achieve internally acceptable agreement between the four transducers. The acceptable data is then entered into a Matlab code that subtracts the average velocity determined by the timing method (described in the next section) from each ADCP measured velocity to determine the error of each bin velocity. These errors are then tracked on X and R_m control charts.

X and R_m control charts are used to track the average value and variability of individual measurements. The X chart for this study plots the error of each bin versus the sample number. A mean error is then calculated for k samples by:

$$\bar{X} = \frac{\sum_{i=1}^{k} X_i}{k} \tag{1.1}$$

Typically, an R chart is used to obtain the variance of a set of data. Each point on an R chart represents the range of a measurements in a sample. Since the data points in this analysis only contain a single measurement the R_m (moving range) chart is used in place of the standard R chart. Each bin velocity is considered to be independent in space and time. The run samples are divided into overlapping subgroups and the range of each subgroup is plotted on the R_m chart. It is important for the size of the subgroups to be small. This analysis uses a subgroup size $n = 3$. For k samples with subgroup size n, the R_m chart contains $(k - n + 1)$ data points. The average sample moving range is calculated by:

$$\bar{R}_m = \frac{\sum_{i=1}^{k-n+1} R_{m_i}}{k - n + 1} \tag{1.2}$$

The standard deviation for the error of the run is then estimated by:

$$\hat{\sigma}_X = \frac{\bar{R}_m}{d_2} \tag{1.3}$$

where d_2 is a constant corresponding to a sample size of 3. Finally the variance for the run is calculated as the standard deviation squared. The control limits are determined by the standard deviation. [3]

It should be noted again that bad bins are not considered here. This analysis only considers what the ADCP deems good data and the bad bins are simply passed over since the analysis assumes that each sample is independent.

1.3 Analysis of Time Based Velocity Measurements

The experimental setup is such that the ADCP measured velocities are correlated against the speed of a raft on which it is mounted. The raft is driven at a constant speed by reeling in a tow line using an electric motor governed by a variable speed controller. The speed is calculated by measuring the time the raft takes to travel between two markers set 50 ft apart. The technician recording the time starts and stops the timer as a common point on the raft passes each marker.

To determine the uncertainty associated with this method a simple uncertainty analysis for product functions can be implemented. Many functions can be expressed as the product of primary dimensions:

$$R = x_1^{a_1} x_2^{a_2} \dots x_n^{a_n} \tag{1.4}$$

Performing the partial differentiations and rearranging terms gives:

$$\frac{\omega_R}{R} = \left[\sum \left(\frac{a_i \omega_{x_i}}{x_i} \right)^2 \right]^{\frac{1}{2}} \tag{1.5}$$

This is the general uncertainty equation for product functions where ω_R is the uncertainty on R and ω_{xi} is the absolute uncertainty on x_i. [6] This general formulation can be applied to analyze the velocity measurements. For:

$$V = xt^{-1} \tag{1.6}$$

The partial derivatives are:

$$\frac{\partial V}{\partial x} = \frac{1}{t} \qquad \frac{\partial V}{\partial t} = -\frac{x}{t^2} \tag{1.7}$$

These partial derivatives can be used derive a specific form of the general uncertainty equation:

$$\partial V = \sqrt{\left(\partial x \frac{\partial V}{\partial x}\right)^2 + \left(\partial t \frac{\partial V}{\partial t}\right)^2}$$

$$\partial V = \sqrt{\left(\partial x \frac{1}{t}\right)^2 + \left(-\partial t \frac{x}{t^2}\right)^2}$$

$$\partial V = \sqrt{\left(\partial x \frac{1}{t}\left(\frac{x}{x}\right)\right)^2 + \left(-\partial t \frac{x}{t^2}\right)^2}$$

$$\frac{\partial V}{V} = \sqrt{\left(\frac{\partial x}{x}\right)^2 + \left(-\frac{\partial t}{t}\right)^2} \tag{1.8}$$

Notice that ω_R and R are replaced by δV and V respectively where $\frac{\delta V}{V}$ is the relative uncertainty of the measurement.

This form can be used to determine the velocity uncertainty, ∂V, based on the resolutions of the distance and time measurands, ∂x and ∂t respectively, and also the measured values of V, x and t.

The time was recorded with a timer accurate to 0.1 seconds over a constant distance of 50 ft with a tape measure accurate to 1/16 in (0.0052 ft). In the first run, the raft took 20.1 seconds to travel the 50 ft resulting in an average constant velocity of 2.49 ft/s. This information is used in the above equation to determine the uncertainty of the velocity measurement:

$$\partial V = V\sqrt{\left(\frac{\partial x}{x}\right)^2 + \left(-\frac{\partial t}{t}\right)^2}$$

$$\partial V = 2.49 \text{ ft/s}\sqrt{\left(\frac{0.0052 \text{ ft}}{50 \text{ ft}}\right)^2 + \left(-\frac{0.1 \text{ s}}{20.1 \text{ s}}\right)^2}$$

$$\partial V = 1.24 \times 10^{-2} \text{ ft/s} \tag{1.9}$$

Therefore, the velocity for the first run is 2.49 ± 0.0124 ft/s. The average uncertainty for all of the runs, based on the resolution of the measurement instruments, is ± 0.0146 ft/s.

The time measurement has an additional source of error since each recorded time is based on a person starting and stopping the timer. Since the decision to start and stop the timer is a bit subjective and the reaction time of the operator can affect the result, it is prudent to consider this source of error from a statistical standpoint.

For the raft testing, two sets of ten runs were performed at the different speed settings. All of the time measurements for each speed setting are grouped together and analyzed using X and R_m charts. Table 1.1 shows the resulting statistics.

Raft Speed Statistics		
Speed Setting	Average Time (sec)	Variance (sec)
6	19.845	0.451
7	17.49	0.268

Table 1.1. Raft Speed Statistics

It can be seen that with the second speed setting, the variance of the time measurement improved. This could be attributed to increased operator experience. Regardless, the variance of the time measurement is greater than the resolution of the stopwatch so this value should be used to determine the overall velocity uncertainty.

$$
\begin{aligned}
\partial V &= V\sqrt{\left(\frac{\partial x}{x}\right)^2 + \left(-\frac{\partial t}{t}\right)^2} \\
\partial V &= 2.49 \text{ ft/s}\sqrt{\left(\frac{0.0052 \text{ ft}}{50 \text{ ft}}\right)^2 + \left(-\frac{0.451 \text{ s}}{20.1 \text{ s}}\right)^2} \\
\partial V &= 5.59 \times 10^{-2} \text{ ft/s}
\end{aligned} \tag{1.10}
$$

1.4 *Results of Open Tunnel Testing*

The data presented in this section comes from the senior design team's first attempt to create a calibration system. The system consisted of a six foot long, thirty inch diameter aluminum tunnel lined with neoprene. The tunnel was submerged and attached to a custom built pontoon boat such that the tunnel would move horizontally through still water. In this way a relative constant flow cross section would be seen by the ADCP which was mounted on the side of the tube looking inward. The neoprene served to prevent reflection of the acoustic signal so that only signal from moving particulate in the water returned to the transducers. The size of the tunnel diameter was necessary to account for the blanking distance of the ADCP. The distance from the transducer faces to the depth of the first observable bin is the blanking distance. Since the ADCP can not instantaneously send and recive an acoustic signal a time delay must occur between these modes of operation and so no data can be captured immediatly in front of the unit.

The transect data for the open tunnel testing resulted in a series of ensembles only one bin deep. This is due to the blanking distance taking up most of the domain inside the tunnel. The transect data is presented in Figure 1.1.

This small piece of the entire transect was considered since it is the longest set of relatively continuous ensembles, that is, there are relatively few bad bins over this section of the data compared to the entire transect. Analyzing this data using the

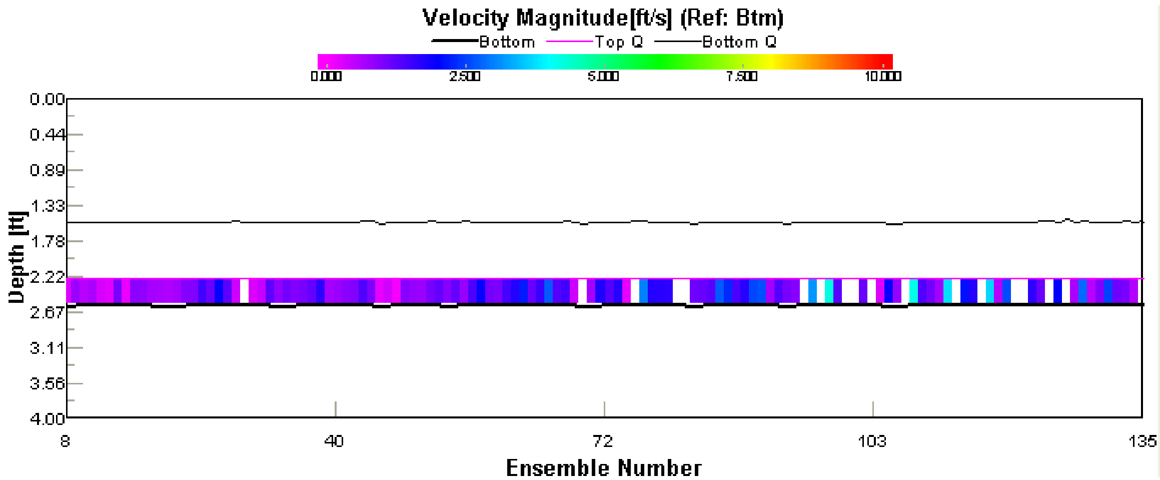

Figure 1.1. Open Tunnel Testing Transect

method described above results in the statistical control chart presented in Figure 1.2.

Comparing the control chart with Figure 1.1, it can be seen that towards the end of the set, the error and range fall outside the control limits. It should be reiterated here that bad bins are not considered and so it seems that good bins which fall around bad bins tend to have more error associated with them even though the ADCP considers them good. In short, more bad bins in the set translate to more error in the good data.

If the data set is truncated so the out of control points are not included, the bias error drops slightly but the variance statistic improves as shown in Figure 1.3.

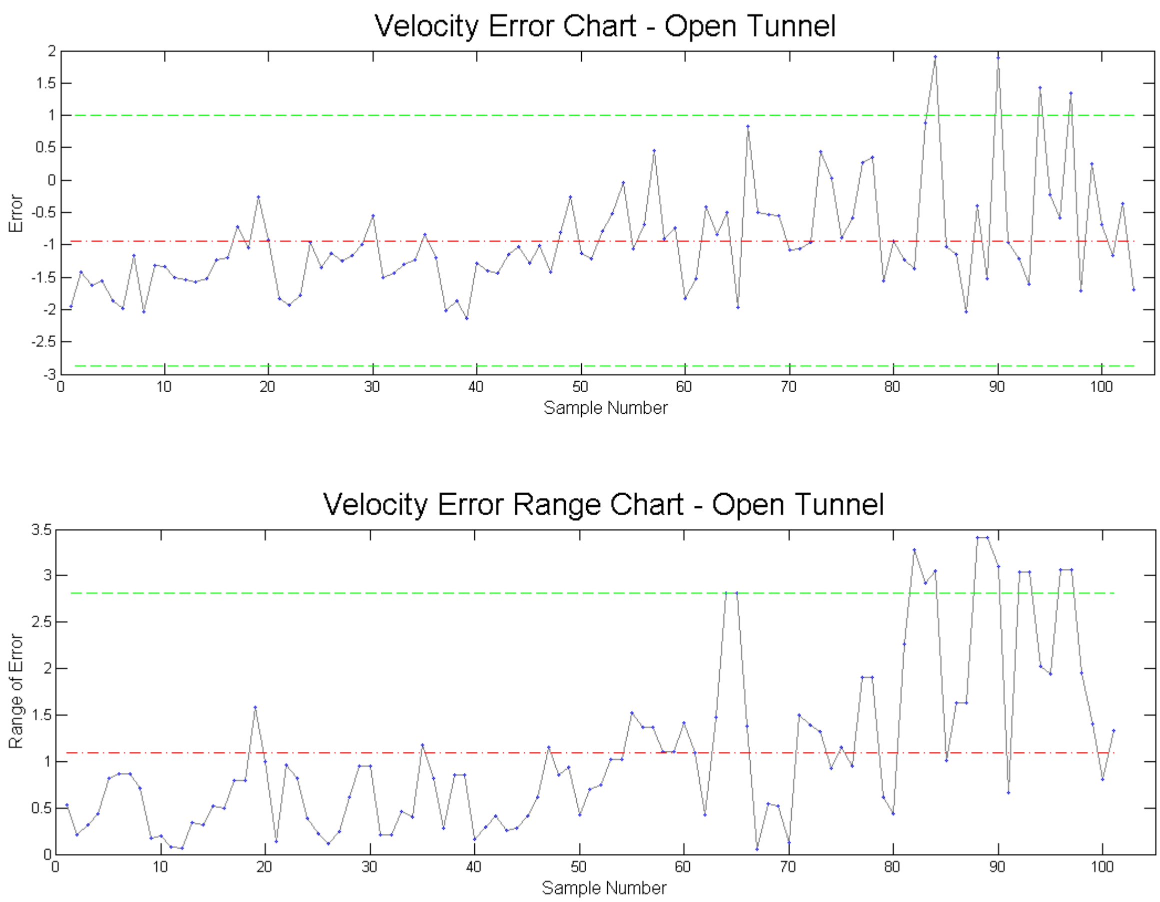

Figure 1.2. Open Tunnel Testing Error Charts

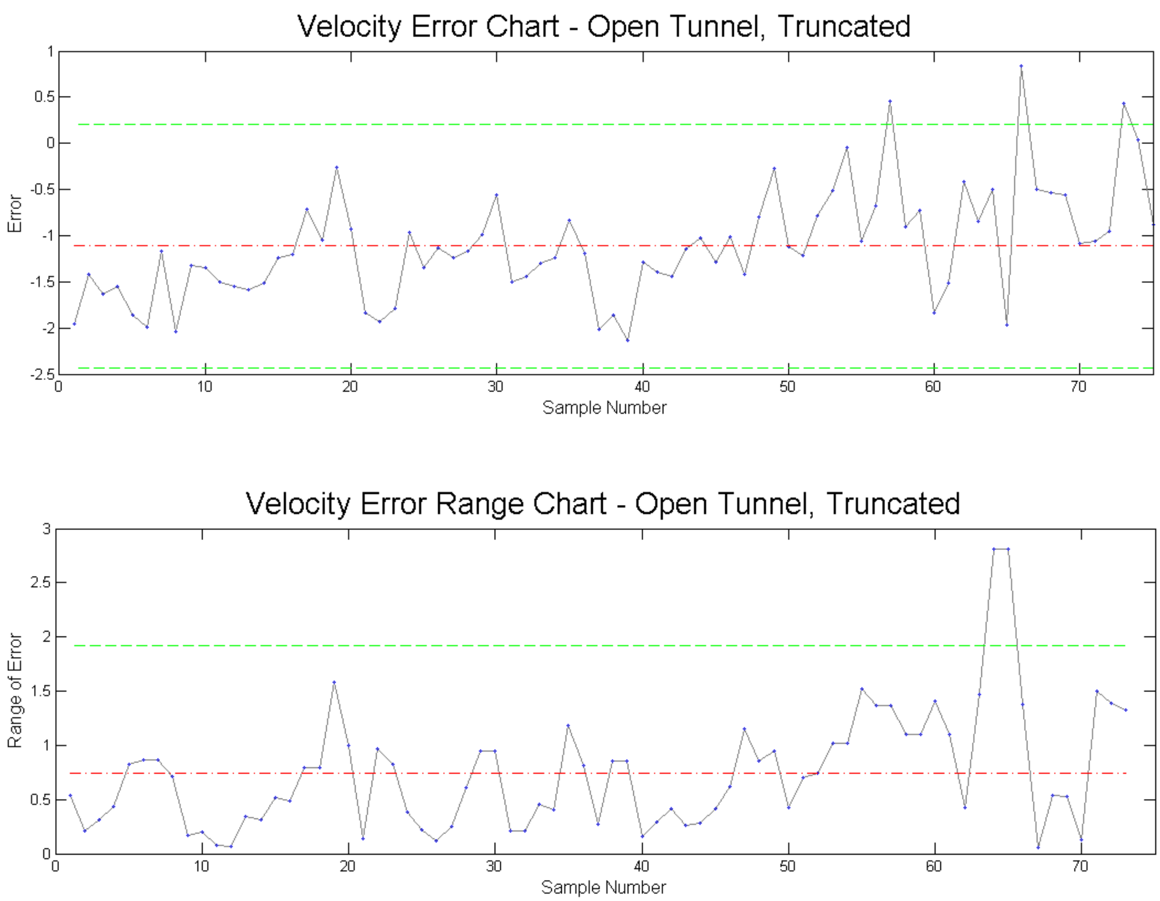

Figure 1.3. Open Tunnel Testing Truncated Error Charts

1.5 Results of Raft Testing

Since the open tunnel testing method proved difficult to produce repeatable data, the decision was made to change to a raft calibration design. These results proved to be repeatable. Four sets of 10 runs of data were performed using varying the speed and configuration setting between two choices each. Transect 1.0 is shown in Figure 1.4. The corresponding control charts for this run is shown in Figure 1.5. This same analysis was performed on each of the 40 transects. The results of the analysis is complied into Table 1.2.

A complete set of control charts is provided in Appendix B. Appendix A provides the Matlab code used to analyze the data and produce the control charts. The raft data appears to be consistent and repeatable. Table 1.3 shows the results in a more concise form along with the settings for each set. For a set speed, the variance is slightly reduced for configuration 2. Also, the bias error increases with velocity given a constant configuration setting.

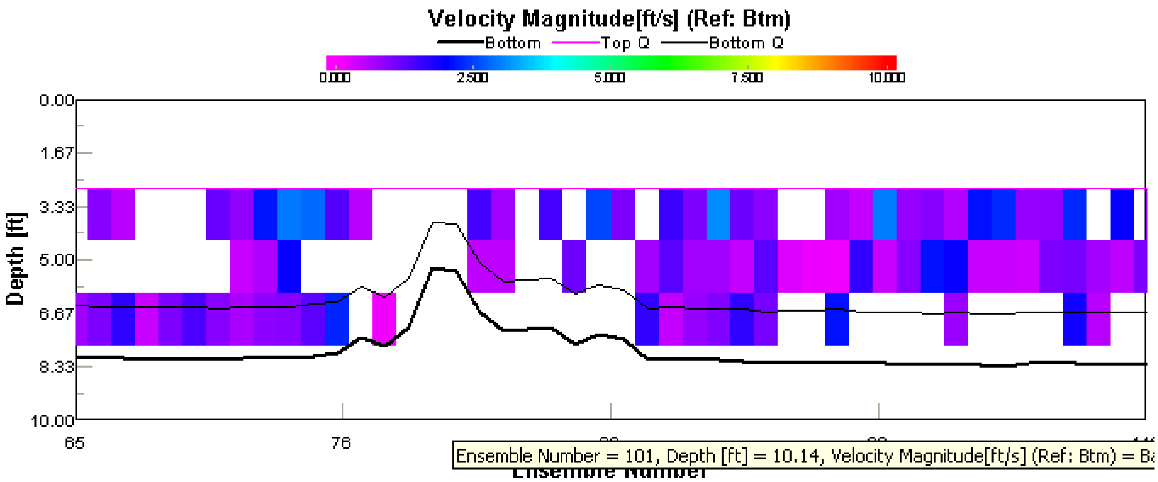

Figure 1.4. Raft Test Transect 1.0

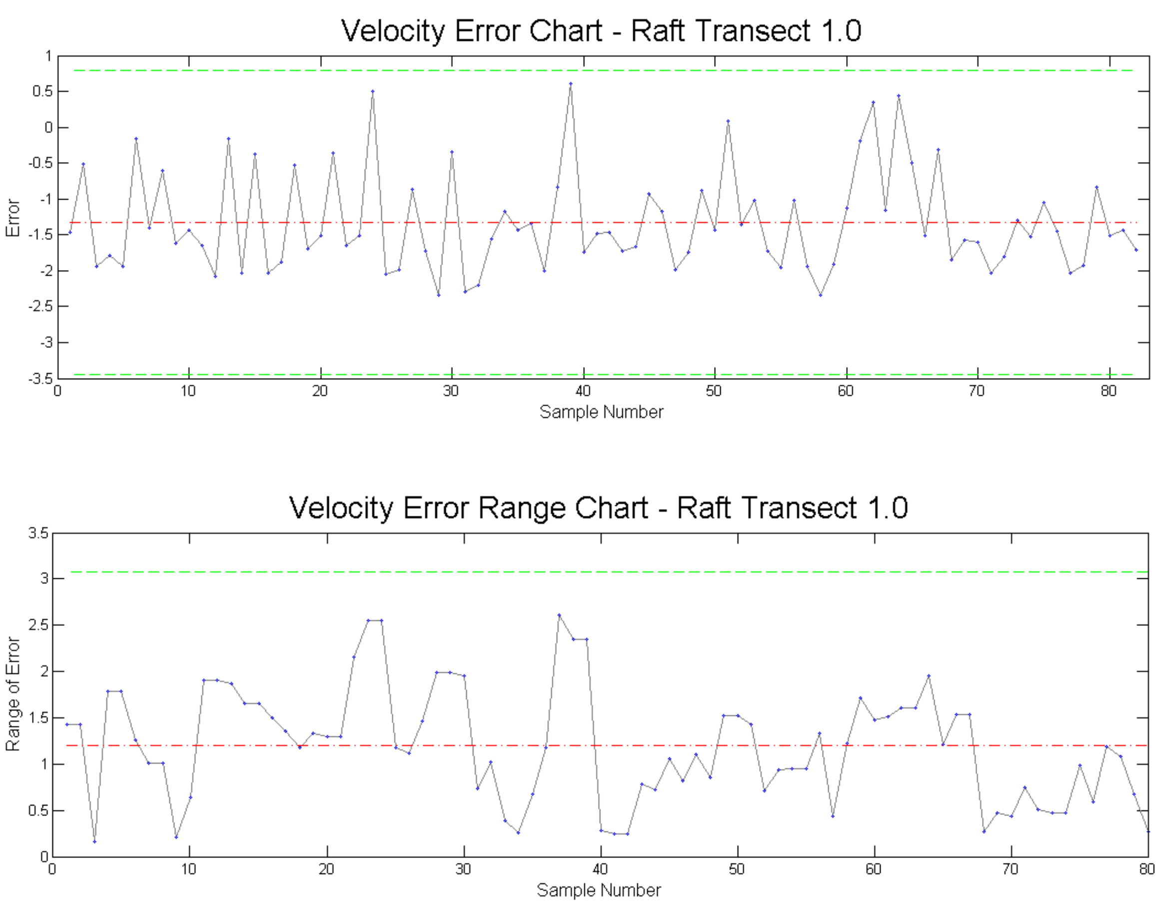

Figure 1.5. Raft Transect 1.0 Error Charts

Table 1.2. Raft Testing Data

	Set 1			Set 2	
run	average error	variance	run	average error	variance
1.0	-1.323	0.499	2.0	-1.460	0.305
1.1	-1.072	0.548	2.1	-1.439	0.327
1.2	-1.349	0.525	2.2	-1.544	0.428
1.3	-1.051	0.978	2.3	-1.474	0.366
1.4	-1.169	0.696	2.4	-1.632	0.314
1.5	-1.414	0.431	2.5	-1.569	0.335
1.6	-1.380	0.528	2.6	-1.233	0.613
1.7	-1.433	0.385	2.7	-1.609	0.349
1.8	-1.279	0.577	2.8	-1.579	0.289
1.9	-1.031	0.509	2.9	-1.590	0.394
Set Average	-1.250	0.567	Set Average	-1.513	0.372
	Set 3			Set 4	
run	average error	variance	run	average error	variance
3.0	-1.588	0.600	4.0	-1.721	0.249
3.1	-1.701	0.437	4.1	-1.651	0.380
3.2	-1.611	0.606	4.2	-1.849	0.455
3.3	-1.673	0.290	4.3	-1.787	0.411
3.4	-1.616	0.505	4.4	-2.035	0.343
3.5	-1.793	0.375	4.5	-1.933	0.439
3.6	-1.604	0.475	4.6	-2.055	0.269
3.7	-1.656	0.516	4.7	-1.989	0.260
3.8	-1.647	0.462	4.8	-1.984	0.188
3.9	-1.773	0.491	4.9	-1.890	0.299
Set Average	-1.666	0.475	Set Average	-1.889	0.329

Table 1.3. Raft Test Settings and Results

Set	Speed Setting	Configuration Setting	Average Error	Variance
1	6	1	-1.250	0.567
2	7	1	-1.513	0.372
3	6	2	-1.666	0.475
4	7	2	-1.889	0.329

1.6 Conclusions

For all of the data analyzed in this report, the bias error is always less than the actual velocity. This is explained by Mueller et al. [9] who shows that the ADCP will always register slower speeds due to downward flow at the forward transducer face and upward flow at the rearward transducer face. For this reason, future testing should include hydrodynamic fairings on the test setup to reduce the flow deflection around the ACDP as much as possible.

These results show a much larger bias error compared to similar tow tank testing. Oberg [10] details tow tank testing performed by the United States Geological Survey and SFWMD at the Naval Center for Surface Warfare in the David Taylor Model Basin in West Bethesda, Maryland. For a 600 kHz ADCP at similar velocities, this study saw a difference of only -0.23 cm/s , a much smaller bias error. There may be several reasons for this including unknown flows in the testing pond, flow anomalies from the raft geometry or towing methods or inappropriate configuration settings for the test.

2. WAVELENGTH TRENDS OF INSTABILITY STRUCTURES IN EVAPORATING LIQUID FILMS

2.1 Introduction to Instability

The stability of a system is determined by its response to a disturbance as it is perturbed from steady state. A system may be classified as stable, unstable, neutral or nonlinearly unstable. A stable system will return to its original steady state regardless of the perturbation. An example of this would be a pendulum. A neutrally stable system will change from its original state given some perturbation but the perturbation will not grow and the system will achieve new steady state. An unstable system will deviate from its original steady state with the onset of any perturbation. The perturbation amplitude will continue to grow in the absence of any damping mechanisms. A nonlinearly unstable system may exhibit stable states for certain disturbances while become unstable for other, larger disturbances. [8]

For the instability studies considered the disturbance shall be described by Eqn (2.1):

$$u(\mathbf{x}, t) = \hat{u}(y)e^{ikx+imz+\sigma t} \tag{2.1}$$

where $\hat{u}(y)$ is the complex amplitude, k and m are real components of the wavenumber and σ, the eigenvalue, is complex as described by $\sigma = \sigma_r + i\sigma_i$.[8] The time constant of Eqn 2.1, σ_r, determines the stability state:

$$\begin{aligned}
\sigma_r > 0 &\longrightarrow \text{unstable} \\
\sigma_r < 0 &\longrightarrow \text{stable} \\
\sigma_r = 0 &\longrightarrow \text{neutrally stable}
\end{aligned}$$

When $\sigma_r = 0$ the system is said to be in the marginal state if it is just between stable and unstable states. With respect to thin films, a small change in flow properties can push the system to the unstable state.

2.2 Experiments

Researchers at the University of Washington have performed experiments to study the instability mechanisms in evaporating thin liquid films. Researchers at Michigan Technological University contributed to the project with analysis of the experimental data and image processing of the Schlieren photographs. The experimental setup

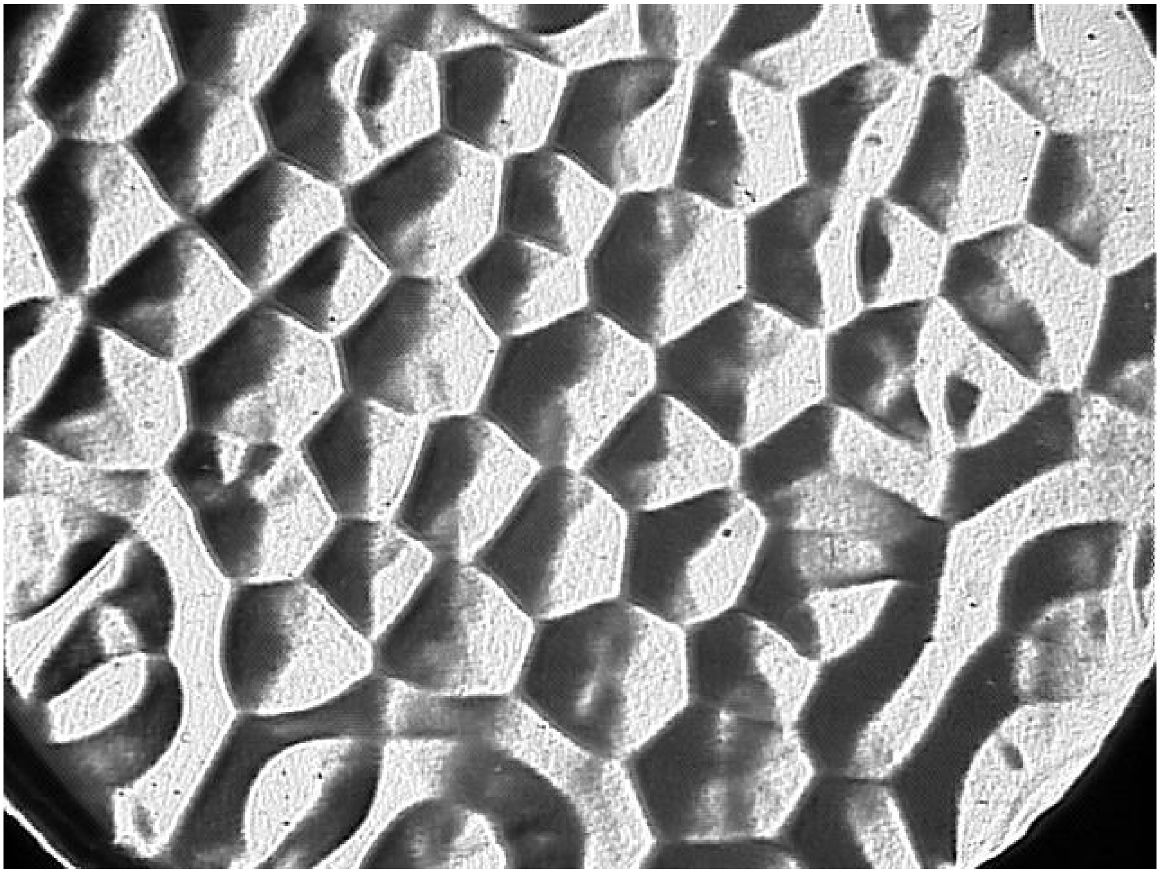

Figure 2.1. Schlieren photograph of instability structures in a thin evaporating film of dichloromethane [7]

consists of a thin liquid film placed on a heated copper block. The film is allowed to evaporate but not boil. The vapor is contained above the film where temperature and pressure are maintained for steady evaporation. Figure 2.1 is an example of the experimental images.[7]

At the onset of instability in the film, the convective cells form. The horizontal distance across each cell is the physical wavelength relating to the fastest growing (critical) wavenumber of the perturbed system.[1] Developing relationships of the critical wavenumber and the other fluid and flow properties is crucial in understanding the phenomenon of evaporating film instabilities.

The images are Schlieren photographs taken at a regular interval to capture density gradients in the film through time. Before presenting more of these photographs, it is prudent to explain how Schlieren works in order to account for visual artifacts in the images.

Many flow phenomena are unobservable to the naked eye but can still be imaged due to the fact that regions of different density affect the local index of refraction in the flow. This bending of light is the basis of the Schlieren family of imaging techniques. These techniques fall in to three main categories: direct shadow, Schlieren and interferometry.

The most basic imaging technique based on variations of refractive index is the direct shadow method. Images are achieved by simply passing light through a flow field of interest and observing the resulting image. Undisturbed light will simply pass through the flow field and image at its nominal intensity. Refracted light however will cast shadows and bright spots on the imaging screen as light passing through areas of higher refractive index will travel more slowly. The observable effects of the direct shadow technique are a function of the second derivative of density. [5]

Schlieren is an extension of direct shadow as this technique serves to separate the refracted light from the undisturbed light by inserting a knife edge at the focal plane before the imaging lens. The knife edge is aligned perpendicular to the density gradient of interest and inserted into the light path to block the undisturbed light. As the undisturbed light is blocked, the overall illumination of the image will be noticeably reduced. At the same time, lines and areas of changing index of refraction show up in striking contrast. The observable effects of the Schlieren technique are a function of the first derivative of density (density gradient). [5]

In Figure 2.1 hexagonal convective cells can be seen here but one should also notice the shadows in each cell. These shadows are an artifact of the Schlieren technique. In fact, the vertical edge of the shadows indicate the orientation of the knife edge as it blocks the undisturbed light. Techniques to remove these shadows are presented further in the thesis.

The convective cells shown in Figure 2.1 are representative of a certain time (film thickness) during the evaporation. As the liquid evaporates and the film thickness decreases, these cell shapes shift about and evolve. Figure 2.2 presents a typical progression of convective structures in the evaporating films. In Figure 2.2a, the evaporating film is relatively thick and just starting to organize into regular cell shapes. As evaporation continues and the film thins, the cells shrink in size and take on a more hexagonal shape as seen in figure 2.2b and figure 2.2c. Near frame 13500, the small wave length begins to appear as ring structures centered about various points shown in figure 2.2d. At this transition a large increase in wave length is observed in the long wave length cell centers and the short wave length structures become more dominate. This continues until the cell centers dissipate and the short wave length remains, as seen in figures 2.2e and 2.2f. The short wave length continues until the film become too thin for the Schlieren to resolve the density gradients. Eventually film rupture occurs. [7]

This trend is common to several different fluids tested. A rather interesting event was captured during an experimental run with methanol as shown in Figure 2.3. The convection cells begin as they did with dichloromethane being rather randomly shaped and dispersed. As the cells shrink in size and become ordered, a transient disturbance occurs in the upper left corner of the image as seen in figure 2.3c. This is likely due to a condensed drop falling onto the evaporating film or a short burst

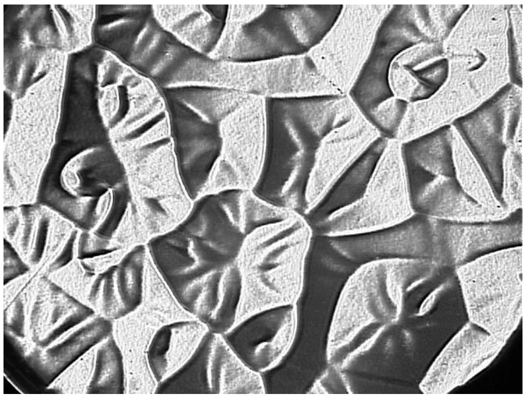

(a) Frame 3000

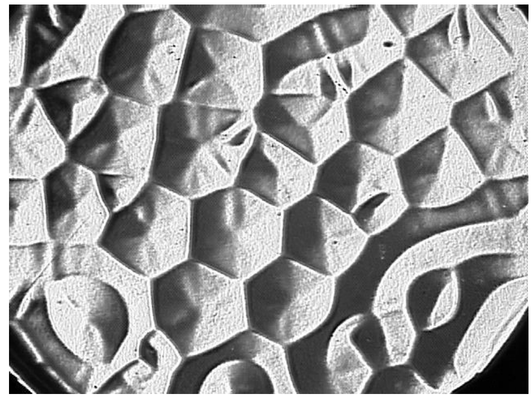

(b) Frame 8000

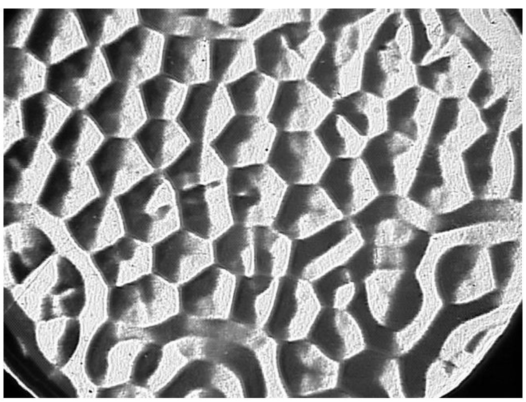

(c) Frame 12000

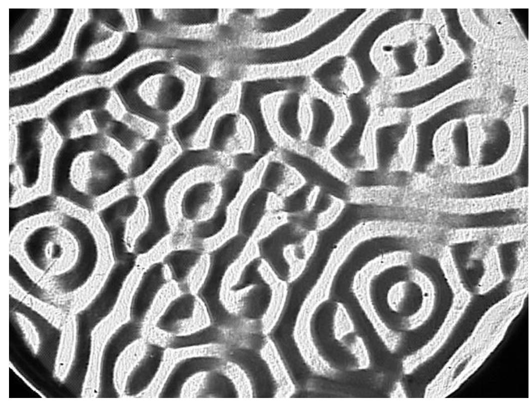

(d) Frame 13500

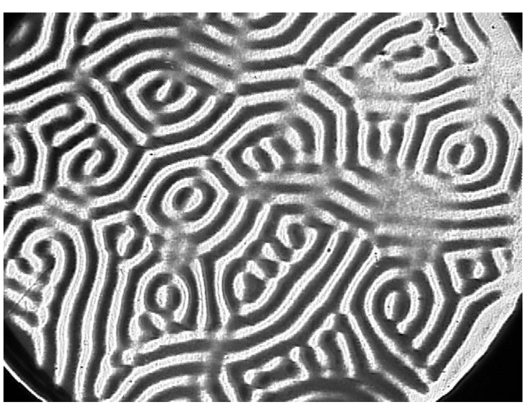

(e) Frame 16000

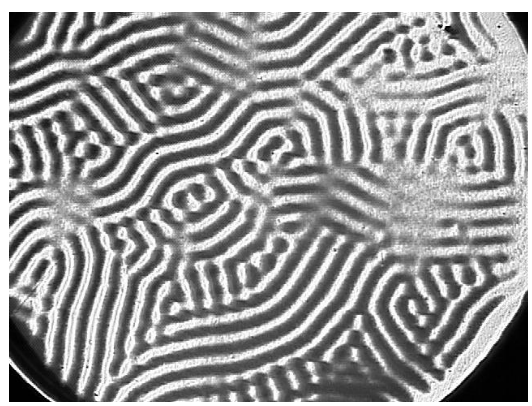

(f) Frame 17000

Figure 2.2. Images from Dichloromethane [7]

of boiling at the edge of film. Interestingly, the disturbance decays quickly and the system seems to recovers to its previous state.

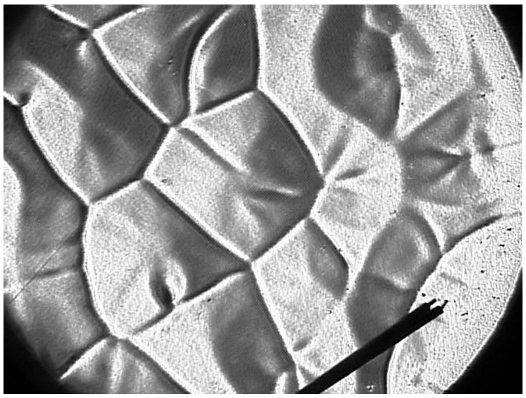

(a) Frame 1500

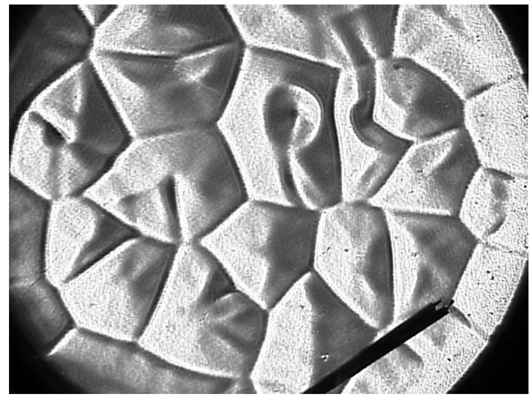

(b) Frame 6000

(c) Frame 9000

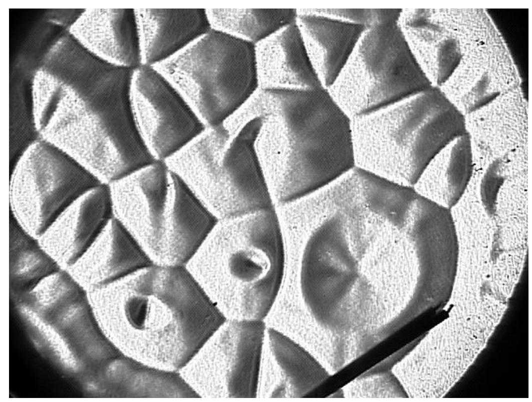

(d) Frame 10000

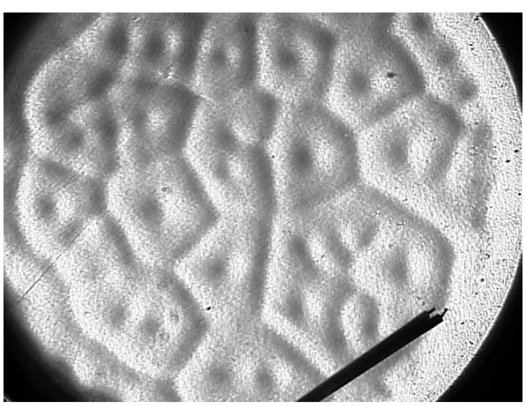

(e) Frame 11100

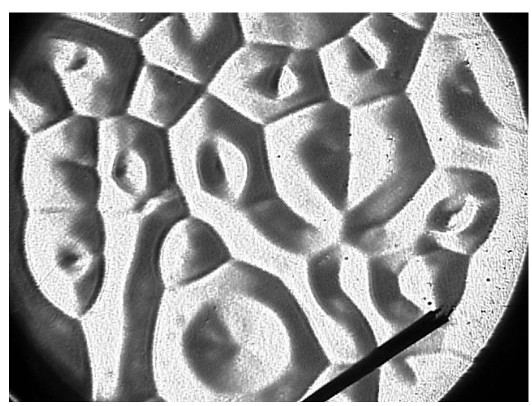

(f) Frame 15000

Figure 2.3. Images from Methanol [7]

2.3 Manually Determining Wavelengths

To extract wavelength information from images where large cells are dominate, the distance between adjacent cell centers is measured manually in Matlab™using the *imtool* command. An example of this is shown below in Figure 2.4. This method suffers in accuracy as estimating the cell centers and trying to randomly pick adjacent cells is somewhat subjective. Nevertheless, wavelengths become quantifiable in time and some striking trends appear as seen in Figure 2.5.

To reduce the error imposed by manually gathering the wavelength data, the following guidelines were followed:

- Measure at least four pairs of cells for each image. The four samples were then averaged together to report a wavelength for the image.
- Sample the most well defined adjacent cell pairs.
- When possible select samples over the entire image.
- If differences in cell size exist, sample from both large and small cell pairs.
- When possible, sample different cell pairs in successive images.

Figure 2.5 shows the results of large wavelength tracking on dichloromethane, images of which can be found in Figure 2.2. The wavelengths decrease as is observed in the images until the dominate structures transition from hexagonal cells to ring structures. The wavelength attributed to the centers of these structures dramatically increases through the transition. This trend continues until the short wavelength becomes entirely dominate.

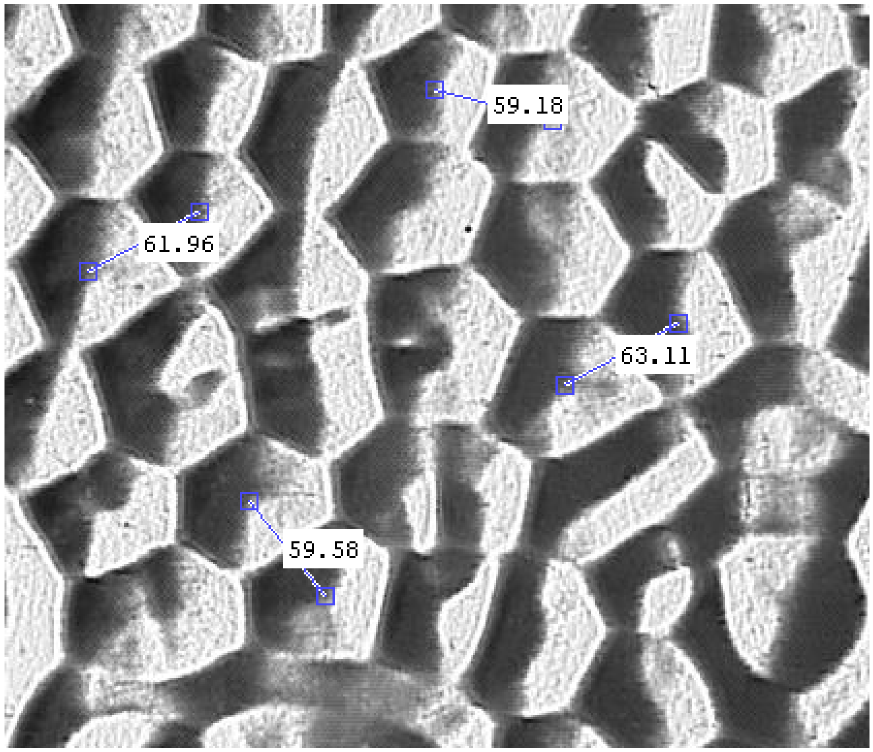

Figure 2.4. Example of manual distance measurement

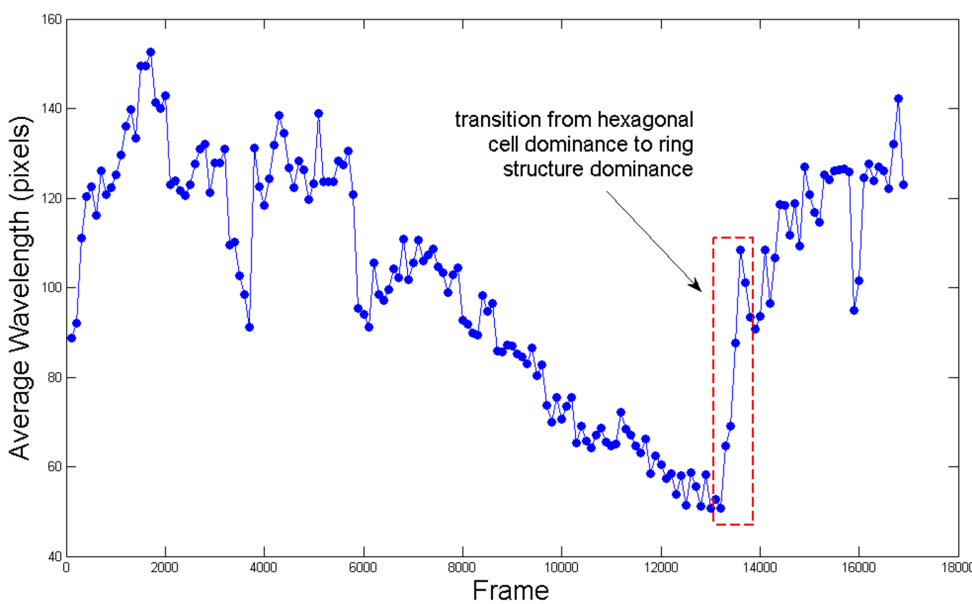

Figure 2.5. Manual wavenumber tracking of dichloromethane

3. IMAGE PROCESSING OF INSTABILITY STRUCTURES IN EVAPORATING LIQUID FILMS

The goal of the image processing is to extract the fastest growing wavelength of instability of an evaporation liquid film. This is found by determining the distance from center to center of neighboring cells in the image. As shown previously, one can manually measure this distance. However, to track this value between many cells per image and over several hundred images is an arduous task. Aside from the tedious nature of doing this manually, picking the exact center of each cell consistently is impossible. The methods aimed at automating the extraction of cell centers and distances are discussed.

3.1 Principle Component Analysis

As an artifact of the Schlieren technique, shadows exist within the pseudo-Bnard cells that hamper the image processing. In an effort to remove these shadows while preserving the cell boundaries, principle component analysis (PCA) is applied. PCA aims to discover what elements of a data set contain interesting dynamics by using the covariance matrix of the data and its corresponding eigenvectors and eigenvalues. The largest eigenvalue of the covariance matrix, with its corresponding eigenvector, represent the first principle component of the data. All subsequent principle components are orthogonal to both the first principle component and each other.[13]

To illustrate how this works, consider a two dimensional point cloud of data points as shown in Figure 3.1a below. This particular point cloud comes from a two dimensional fast Fourier transform of one of the evaporation images being studied. By using PCA, all of the data points are collapsed onto a line in the direction of the most variance. In other words, if one were to draw an ellipse around the point cloud, the data would all collapse onto the major axis of the ellipse.

The first step in PCA is to arrange the data in a matrix where columns will represent dimensions of data and rows represent observations. Since this is a two dimensional point cloud, it is convenient to arrange a 2 by n matrix where the columns are the x and y coordinate and each row is a data point. The matrix must also be centered about zero. This is done for each column by subtracting the column average from each value within the column.

The next step is to calculate the covariance matrix from PCA data matrix. The eigenvalues and corresponding eigenvectors of the covariance matrix are then calcu-

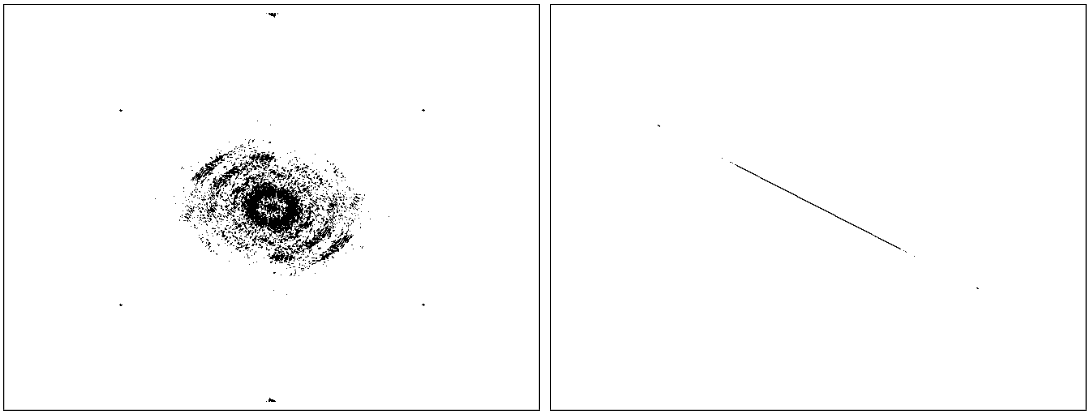

(a) Before PCA (b) After PCA

Figure 3.1. Data point cloud linearized along first principle component

lated. The largest eigenvalue and eigenvector represent the first principle component. The next largest eigenvalue and eigenvector indicates the second principle component and so on. Each principle component is orthogonal to the rest which means in this example, the second principle component represents the minor axis of the hypothetical ellipse bounding the data. Also, since this example started with only two dimensions in the PCA data matrix, only two principle components will result.

The intention is to collapse the data onto a line. Therefore only one of the principle components, the first, will be kept. The eigenvector belonging to the largest eigenvalue becomes the feature matrix or rather the feature vector since only one principle component is retained.

The reduced data is calculated by equation 3.1:

$$[\text{Reduced Data Matrix}] = [\text{Feature Matrix}] * [\text{Original PCA Data Matrix}]' \quad (3.1)$$

The reduced data matrix must then be converted back to the original space by equation 3.2:

$$[\text{Final Data Matrix}] = [\text{Feature Matrix}]' * [\text{Reduced Data Matrix}] \quad (3.2)$$

All that is left is to take the transpose of this matrix and de-center the data by adding the respective column average back to each value. A plot of the resulting points should reveal all of the data collapsed onto a line representing the first principle component as shown in Figure 3.1b:

The basic strategy described above can be applied to a series of images to extract features that are common between them. This is referred to as sequence principle component analysis (SPCA) in this report. In SPCA, the extraction of principle components is the same as in PCA however the setup of the original data matrix is different. Each image is rearranged into a single vector by moving to the right across

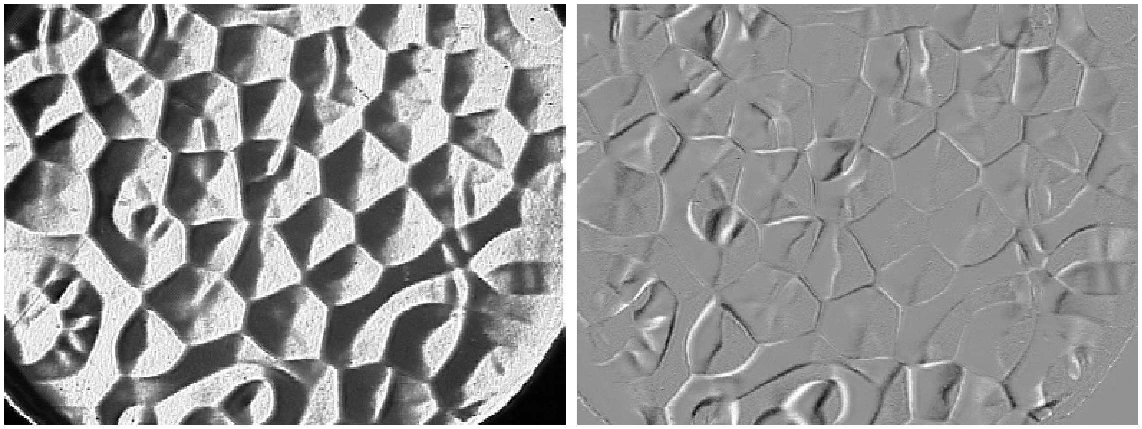

Figure 3.2. Original image (left) and the second principle component of the same image (right)

the photograph and stacking each column of pixel data below the previous column. This is done for a series of images captured close in time and each image vector becomes a dimension (column) in the PCA data matrix. The number of images used determines the number of principle components that can be extracted.

Once the images have been rearranged and assembled into the PCA data matrix, the data matrix is centered and run through the analysis described above. The desired principle components are selected that produce the best image of cell boundaries only and the images are rebuilt from the resulting final principle component data matrix. The principle components used in the feature matrix are selected by trial and error method. The number of images used in the SPCA affect which components to extract.

An example of the results of this technique along with the original image is shown below in Figure 3.2. The cell boundaries are preserved with the second principle component of the image while the shadows, along with much of the noise, are reduced or eliminated.

The cell boundaries which are the features of interest, are preserved while eliminating much of the shadows and noise. This simplified image will be much easier to use in further image processing techniques.

3.2 Wavelength Extraction in the Frequency Domain

To extract the wave number automatically, Matlab™code has been written that combines two dimensional fast Fourier transforms with two dimensional principle component analysis. The following steps are used to extract the frequencies from an image:

1. A gray-scale image of interest is loaded into the program workspace. needs to be a gray scaled intensity image.

2. The image is windowed and transformed via two-dimensional Fast Fourier Transform. The resulting data is shifted so the zero frequency is located in the center.

3. The amplitudes are scaled by the log of the absolute value. An adjustable threshold is defined as a percentage of the max amplitude. Any data falling below this threshold is ignored. This energy filter converts the FFT image to binary.

4. Two-dimensional principle component analysis is performed on the resulting point cloud to collapse the data onto the first principle component. This identifies the direction accounting for the largest variance in the point cloud.

5. The Euclidean distance of each point on the first principle component is determined.

6. The number of points at each distance (frequency) is determined and plotted.

7. The highest occurring frequency is extracted from the plot.

Figure 3.3 shows the results of this process. The reported frequency for this image is 26.5 pixels. Figure 2 shows a comparison of this result to pixel measurements performed on the original image.

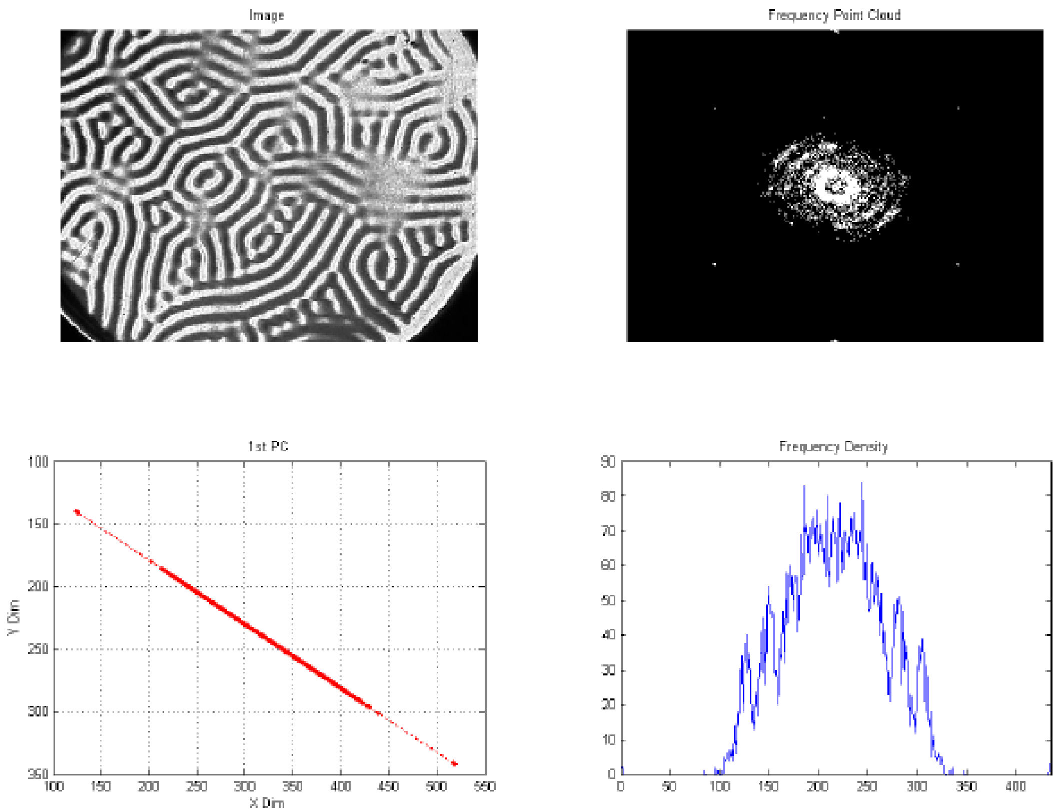

Figure 3.3. Example result of automated wavelength extraction

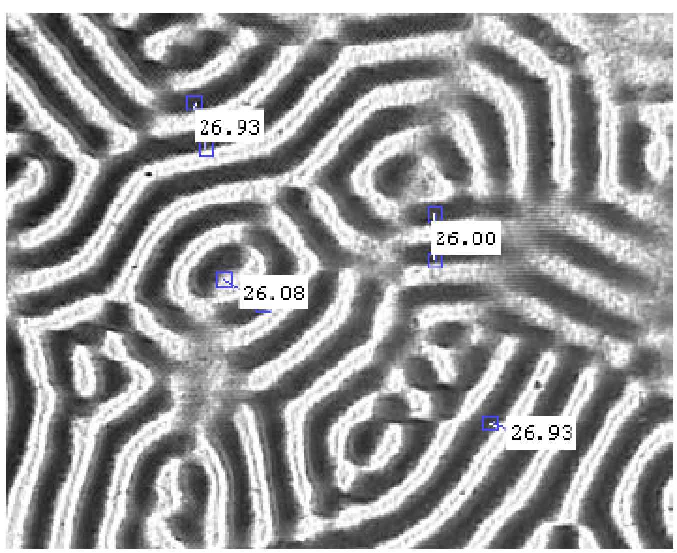

Figure 3.4. Manual measurement of same image processed in Figure 3.3

3.3 Results of Image Processing

The goal of the image processing work was to create a program that would automatically extract wave length information from Schlieren images of an evaporating film. The approach taken was to use two dimensional fast Fourier transform (FFT) to identify features of interest in the frequency domain. This effort was met with mixed success. Images of the film where large cells, random or ordered, were dominant did not produce enough repeating features in any one direction to be detectable by the two dimensional FFT method. As the smaller wave lengths become prevalent, that is, when the ring structures form and become dominate, the FFT picks up these highly repeating structure quite well.

To extract the wave lengths from the large cell patterns, dedicated image processing software may be needed. The SPCA method applied to the images greatly reduces the large Schlieren shadows in the center of the cells and highlights the cell boundaries. This will aid image processing in other third party software.

4. BEHAVIOR OF THE CRITICAL WAVENUMBER IN A ONE SIDED EVAPORATION MODEL

4.1 The Rayleigh Bénard Problem

One of the most well known instability problems in thin film fluid mechanics is the Bénard Problem. The experiment, conducted by Henri Bénard in 1900, involved heating a thin film from below to create a thermal gradient resulting in cooler, top heavy fluid above the warmer fluid layers. Ordered hexagonal convection cells developed with the onset of the instability once the temperature gradient became sufficiently large. A sketch of the problem is shown in Figure 4.1. In 1916, Lord Rayleigh defined a non-dimensional ratio of fluid properties where, at a critical value of this ratio, the convective cells observed by Bénard develop.[8] This ratio, known as the Rayleigh Number.

$$Ra = \frac{g\alpha\Gamma d^4}{\kappa\nu} \sim \frac{\text{Buoyancy Force}}{\text{Viscous Force}} \tag{4.1}$$

where g is the acceleration due to gravity, α is the coefficient of thermal expansion, $\Gamma = -d\bar{T}/dz$ is the vertical temperature gradient of the initial state, d is the depth of fluid at the initial state, κ is the thermal diffusivity and ν is the kinematic viscosity. [8] Convective cells observed by Bénard's experiments are driven by surface tension variations due to temperature.

In the next section, the discussion considers the validity of an assumption on the critical wavenumber in Padate's thesis[12] therefore it is important to establish a

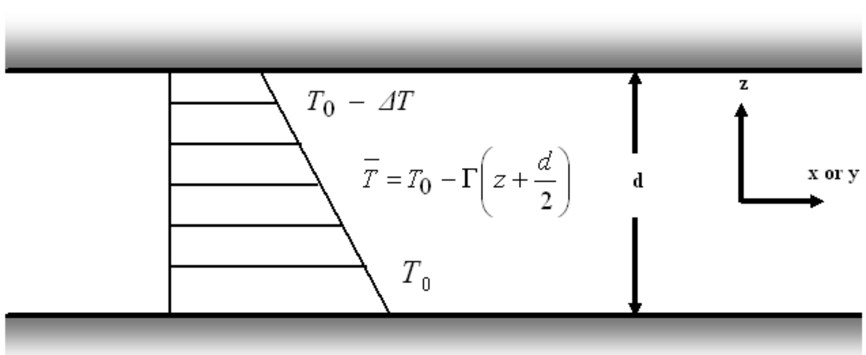

Figure 4.1. Unstable initial conditions which will lead to convection

foundation of its derivation and implication to film instability. Kundu's derivations of Bénard convection will be followed to accomplish this.

Kundu begins with the Boussinesq approximation of the continuity, momentum and heat equation governing the fluid behavior. These equations are shown below as Eqn 4.2.

$$\begin{aligned}
&\text{Continuity:} && \frac{\partial \tilde{u}_i}{\partial \tilde{x}_i} = 0 \\
&\text{Momentum:} && \frac{\partial \tilde{u}_i}{\partial t} + \tilde{u}_j \frac{\partial \tilde{u}_i}{\partial x_j} = -\frac{1}{\rho_0}\frac{\partial \tilde{p}}{\partial x_i} - g[1-\alpha(\tilde{T}-T_0)]\delta_{i3} + \nu\nabla^2\tilde{u}_i \\
&\text{Energy:} && \frac{\partial \tilde{T}}{\partial t} + \tilde{u}_j \frac{\partial \tilde{T}}{\partial x_j} = \kappa\nabla^2\tilde{T}
\end{aligned} \tag{4.2}$$

The Boussinesq approximation is such that density, ρ, is treated as a constant in all terms except the external force term.[1] The dimensional variables represent the variables in the initial state in the manner of Kundu.[8] Density is given by the equation of state Eq(4.3) :

$$\tilde{\rho} = \rho_0[1-\alpha(\tilde{T}-T_0)] \tag{4.3}$$

The full derivation of the evolution equation has been presented in chapter 11 of Kundu.[8] The momentum variables are represented as a base state plus a perturbation which is applied to the model presented in Figure 4.1. The equations are linearized and the Prandlt number, Rayleigh number and wavenumber appear as key parameters in the dimensionless linearized equantions which constitute an eigenvalue problem for the time constant σ.

Solving this problem for the flow between two rigid plates, as shown in Figure 4.1 yields an eigenvalue problem of a sixth order. The solution to this problem yields a relationship between Ra and K where a minimum value for Ra exists at the onset of instability. This critical Rayleigh Number, Ra_{cr}, has a corresponding critical wavenumber, K_{cr}. ($K = \sqrt{k^2 + l^2}$). For this case $Ra_{cr} = 1708$ and $K_{cr} = 3.12$.[8]

If the boundary conditions are changed, the critical Rayleigh Number and corresponding critical wavenumber will change as well. For the case of a slip boundary condition, where two fluids of different density are superposed between the plates, the heavier on the bottom, the critical Rayleigh number for the heavier fluid and corresponding critical wavenumber become $Ra_{cr} = 657$ and $K_{cr} = \pi/\sqrt{2}$ respectively.[8] This relationship is shown in Figure 4.2.

The value of K_{crit} will change if the boundary conditions of the system are also changed.

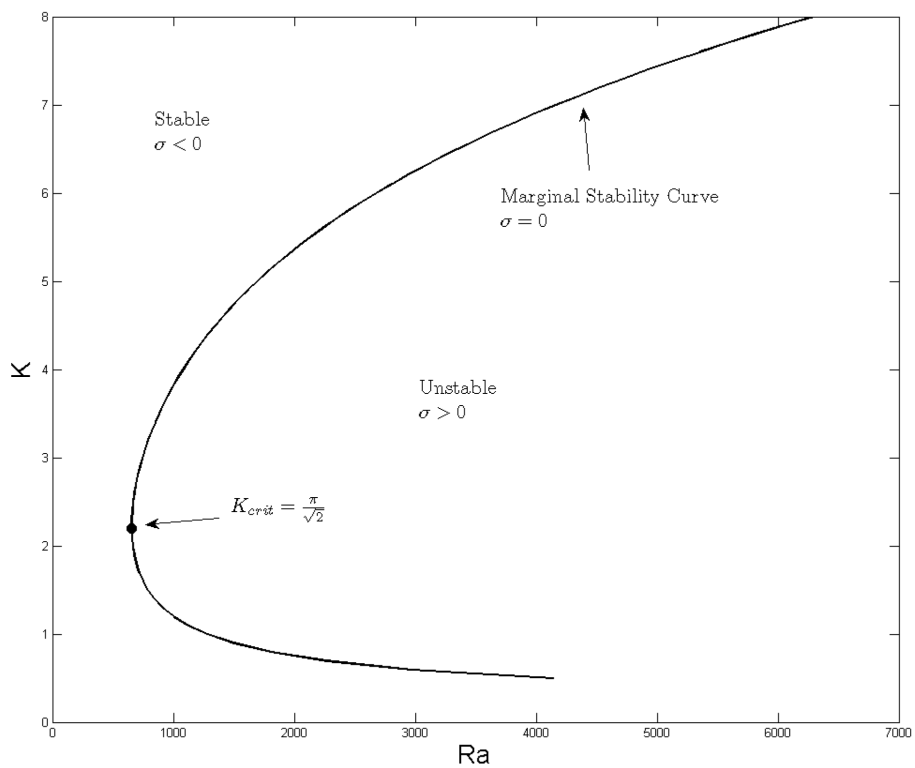

Figure 4.2. Stable and unstable regions for Bénard convection with free surface

4.2 A One Sided Evaporation Model and the Critical Wave Number

The previous section followed Kundu's formulation [8] of the Bénard problem where the film is bounded below with a no slip surface on top by a free surface. The solution produced a stability relationship between the wavenumber and the Rayleigh number. With a basic understanding of film instability established, the discussion moves to validate or revise the assumption that for a given evolution equation, the critical wavenumber stays constant. The one sided evaporation model was proposed by Davis [2] for film rupture studies and investigated further by Padate [12] with numerical simulation in which he solved multipule cases, turning terms off and on in the evolution equation. The previous section inferred that if the boundary conditions change, so will the critical wavenumber for the classical Rayleigh-Bénard problem. The following discussion will analytically show that changes in fluid and flow properties can change the critical wavenumber.

The one sided evolution equation for an evaporating liquid film proposed by Davis [2] and studied by Padate [12] is shown in Eqn 4.4:

$$
\begin{aligned}
0 = h_t + \frac{Eh}{h+K} + S(h^3 h_{xxx})_x \\
+ \left\{ \left[Ah^{-1} - Gh^3 + E^2 D^{-1} \left(h + K^{-1}\right) h^3 + \frac{KMh^2}{P\,(h+K)} \right] h_x \right\}_x
\end{aligned}
\tag{4.4}
$$

where S is the non-dimensional surface tension. Other non-dimensional terms include A, accounting for van der Waals attractions; P, the Prandtl number; E, the evaporation number; D, the density ratio; M, accounting for thermo capillary flows; K, a measure of non-equilibrium at the interface; and G, the gravitational number. The reader is referred to Padate for details.[12].

Linearization of this equation about $h = 1$ yields Eqn 4.5. It should be noted that $\frac{EH}{h+K}$ is not 0 when $h = 1$ so no bifurcation presents if E $O(1)$. If E is sufficiently small, this term is dropped [11] yet the $\frac{E^2}{D}$ term is retained because it bay be $O(1)$.

$$
0 = \frac{\delta H}{\delta t} + \beta H'' + SH'''' \tag{4.5}
$$

where β is defined by

$$
\beta = A - G + \frac{E^2}{D\,(1+K)} + \frac{KM}{P\,(1+K)^2}
$$

Substituting in the perturbation as an initial condition (Eqn 4.6)

$$
H(X,T) = H_0 e^{\omega T + iqX} \tag{4.6}
$$

where ω and q are the perturbation time constant and wavenumber respectively and are equivalent to Kundu's[8] σ and k. This gives the characteristic equation:

$$0 = \omega + Sq^4 - \beta q^2 \tag{4.7}$$

The E term here is very small so it is dropped from the equation [11] yet the E^2 term in β must be retained giving Eqn 4.8:

$$\omega = q^2 \left(\beta - Sq^2\right) \tag{4.8}$$

Padate[12] showed a similar result for an isothermal thin liquid film where:

$$\frac{\beta}{S} = 1 \tag{4.9}$$

and so

$$\omega = q^2 \left(1 - q^2\right) \tag{4.10}$$

The neutral stability curve for this isothermal case is presented in Figure 4.3.

Padate used this critical wavenumber, derived from the isothermal case for all cases tested numerically. The following scaling analysis shows how, for the isothermal case, the β S ratio equals one.

Arbitrary scaling factors are assigned for the x and t variables:

$$\bar{x} = \lambda x \qquad \bar{t} = \Omega t \tag{4.11}$$

The partial derivatives are then derived:

$$\frac{\delta}{\delta t} = \frac{\delta \bar{t}}{\delta t}\frac{\delta}{\delta \bar{t}} \qquad \frac{\delta}{\delta x} = \frac{\delta \bar{x}}{\delta x}\frac{\delta}{\delta \bar{x}} \tag{4.12}$$

$$\frac{\delta}{\delta t} = \Omega\frac{\delta}{\delta \bar{t}} \qquad \frac{\delta}{\delta x} = \lambda\frac{\delta}{\delta \bar{x}} \tag{4.13}$$

Substituting this into the linearized evolution equation for the isothermal case[12] gives:

$$\Omega H_{\bar{t}} + \beta\lambda^2 H_{\bar{x}\bar{x}} + S\lambda^4 H_{\bar{x}\bar{x}\bar{x}\bar{x}} = 0 \tag{4.14}$$

For the coefficients of $H_{\bar{x}\bar{x}}$ and $H_{\bar{x}\bar{x}\bar{x}\bar{x}}$ to be equal gives:

$$\beta\lambda^2 = S\lambda^4 \tag{4.15}$$

$$\beta = S\lambda^2 \tag{4.16}$$

so

$$\beta\lambda^2 = \frac{\beta^2}{S} = S\lambda^4 \tag{4.17}$$

and 4.14 becomes

$$\frac{\Omega S}{\beta^2} H_{\bar{t}} + H_{\bar{x}\bar{x}} + H_{\bar{x}\bar{x}\bar{x}\bar{x}} = 0 \tag{4.18}$$

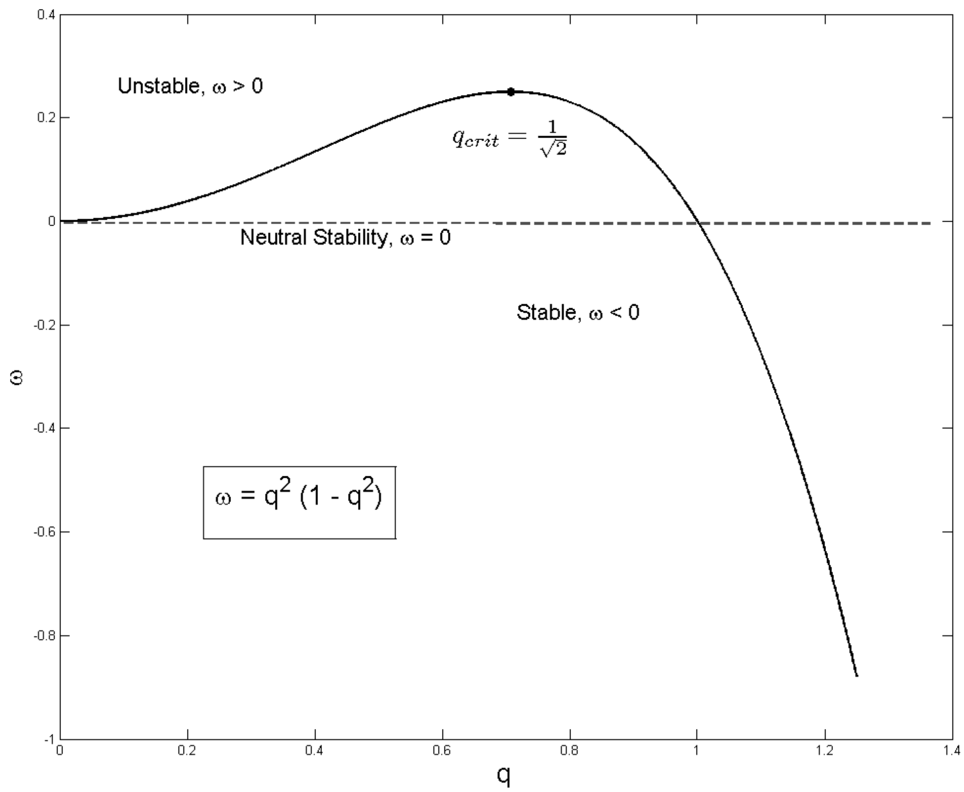

Figure 4.3. Neutral stability curve for the isothermal case

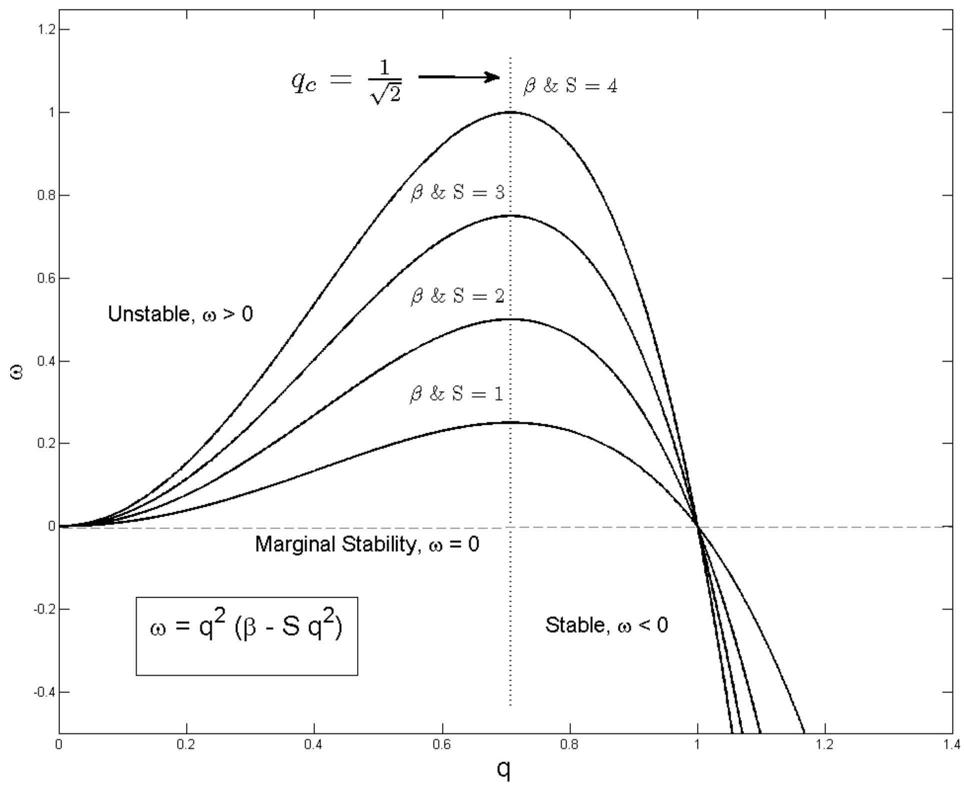

Figure 4.4. Neutral stability curve where $\frac{\beta}{S} = 1$

so Ω is choosen to be

$$\Omega = \frac{\beta^2}{S} \tag{4.19}$$

and finally

$$H_{\bar{t}} + H_{\bar{x}\bar{x}} + H_{\bar{x}\bar{x}\bar{x}\bar{x}} = 0 \tag{4.20}$$

This shows that the isothermal case can be scaled such that the β S ratio is one. So long as this ratio is preserved, the critical wave number will not change as illustrated in Figure 4.4.

The investigation can not stop here however. Turning terms in β on and off will clearly change β however, with respect to given fluid, S will hardly change at all. This means that the β S ratio equal to one will not hold beyond the isothermal case. The effects of this changing ratio are illustrated in Figure 4.5.

Clearly, the assumption that the critical wavenumber of $\frac{1}{\sqrt{2}}$, derived from the isothermal case, applies to any case based from the general evolution Eqn 4.4 does not hold. For each case, β must be calculated to determine the appropriate critical wavenumber.

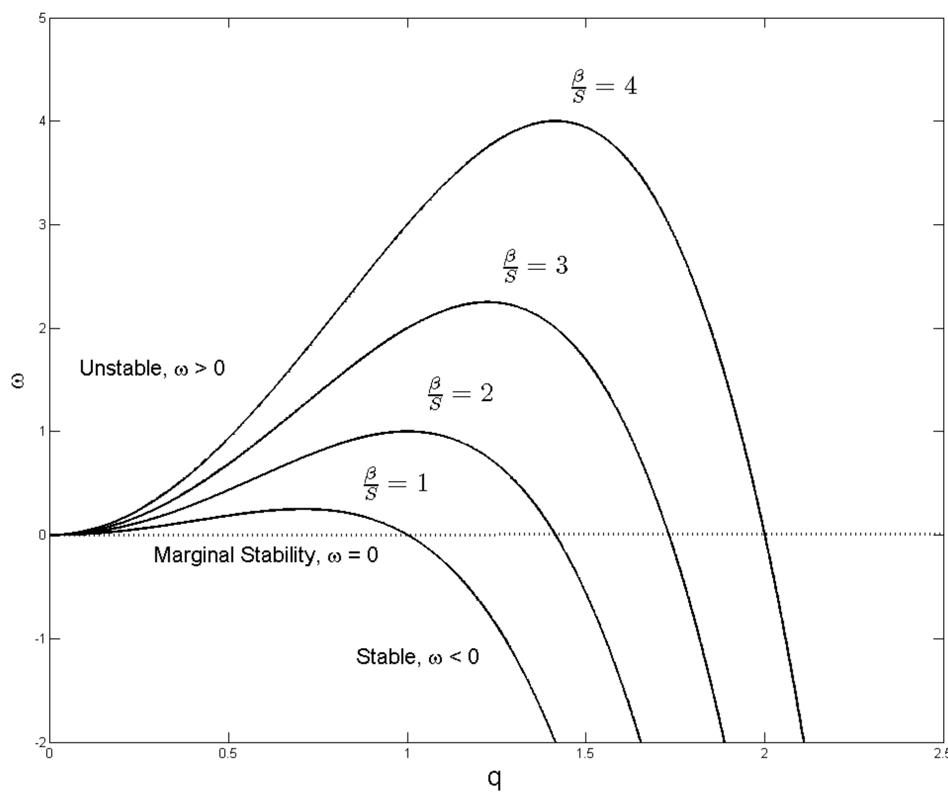

Figure 4.5. Neutral stability curve where $\frac{\beta}{S}$ changes

4.3 Conclusions and Remarks

While working on completing a master of science in mechanical engineering, this author has worked on many different projects and has gained much research experience. The author conducted research on two different projects: calibration of an acoustic Doppler current profiler and investigations of the critical wave number in unstable evaporating thin films. The nature of the work contained herein is widely varied involving experimental setups, data acquisition, statistical analysis, analytical investigation, literature review and computational analysis. The common theme with all of the project work is the investigation and research on thermo fluids with accompanying statistical and analytical analysis.

A notable point about this research is the mixed amount of success and closure of the different tasks. This speaks to the nature of research. The ADCP project is a clear example of the challenges that arise and adaptations that must take place in experimental work. The pontoon driven tunnel system had limited success so the setup was changed to a towed raft design. While still not perfect, this design change significantly improved the data. It also shows that a carefully designed and constructed experiment is every bit as important to the results as the analysis.

In the thin film instability work, the author was able to correct the assumption that the critical wavenumber used in Padate's analysis [12] is not constant. While a conclusive result was found for the analytical work, a complete program for wavenumber extraction was not fully implemented. Incremental advances toward this goal were however achieved in the application of principle component analysis and two dimensional FFT. In research, some problems can be solved directly with the application of theory and cleverness while others require incremental advancements and much adaptation.

The author hopes that this work helps to advance the research he took part in as well as provides examples of the experience and knowledge gained during his time as a master student at Michigan Technological University.

APPENDIX

A. ADCP APPENDICIES

A.1 ADCP - Analysis Matlab Code

```
%ADCP Analysis
%11/14/08
clear, clc, close all
A = xlsread('data_1_0.xls',1,'A1:A150');
B = xlsread('data_1_0.xls',1,'B1:B150');
C = A - B;
k = length(C);
C_bar = sum(C)/k;
C_bar_p = ones(k,1) .* C_bar;
n = 3;
m = 0;
for i = 1:k-2
    sample = [C(2-1+m),C(2+m),C(2+1+m)];
    R_m(i) = max(sample) - min(sample);
    m = m+1;
end
R_m_bar = sum(R_m)/(k-n+1);
R_m_bar_p = ones((k-n+1),1) .* R_m_bar;
R_m_UCL = 2.575 * R_m_bar;
R_m_UCL_p = ones((k-n+1),1) .* R_m_UCL;
stdev = R_m_bar/1.693;
C_UCL = C_bar + (3*stdev);
C_UCL_p = ones(k,1) .* C_UCL;
C_LCL = C_bar - (3*stdev);
C_LCL_p = ones(k,1) .* C_LCL;
disp('The Average Error is:')
C_bar
disp('Plus or Minus')
(stdev^2)
subplot(2,1,1)
sample_no = [1:1:k];
plot(sample_no,C,'-ob',sample_no,C_bar_p,'-.r',sample_no,C_UCL_p,'--g',
   sample_no,C_LCL_p,'--g')
%ylim([-0.25 0.25])
title('Velocity Error Chart')
xlabel('Sample Number')
ylabel('Error')
legend('Data','Average Error','Control Limit','Location','BestOutside')
subplot(2,1,2)
sample_no = [1:1:(k-n+1)];
plot(sample_no,R_m,'-ob',sample_no,R_m_bar_p,'-.r',sample_no,R_m_UCL_p,'
   --g')
%ylim([0 0.3])
title('Velocity Error Range Chart')
xlabel('Sample Number')
ylabel('Range of Error')
legend('Data','Average Error Range','Control Limit','Location','
```

```
BestOutside')
```

A.2 ADCP - Raft Testing Data Set Control Charts

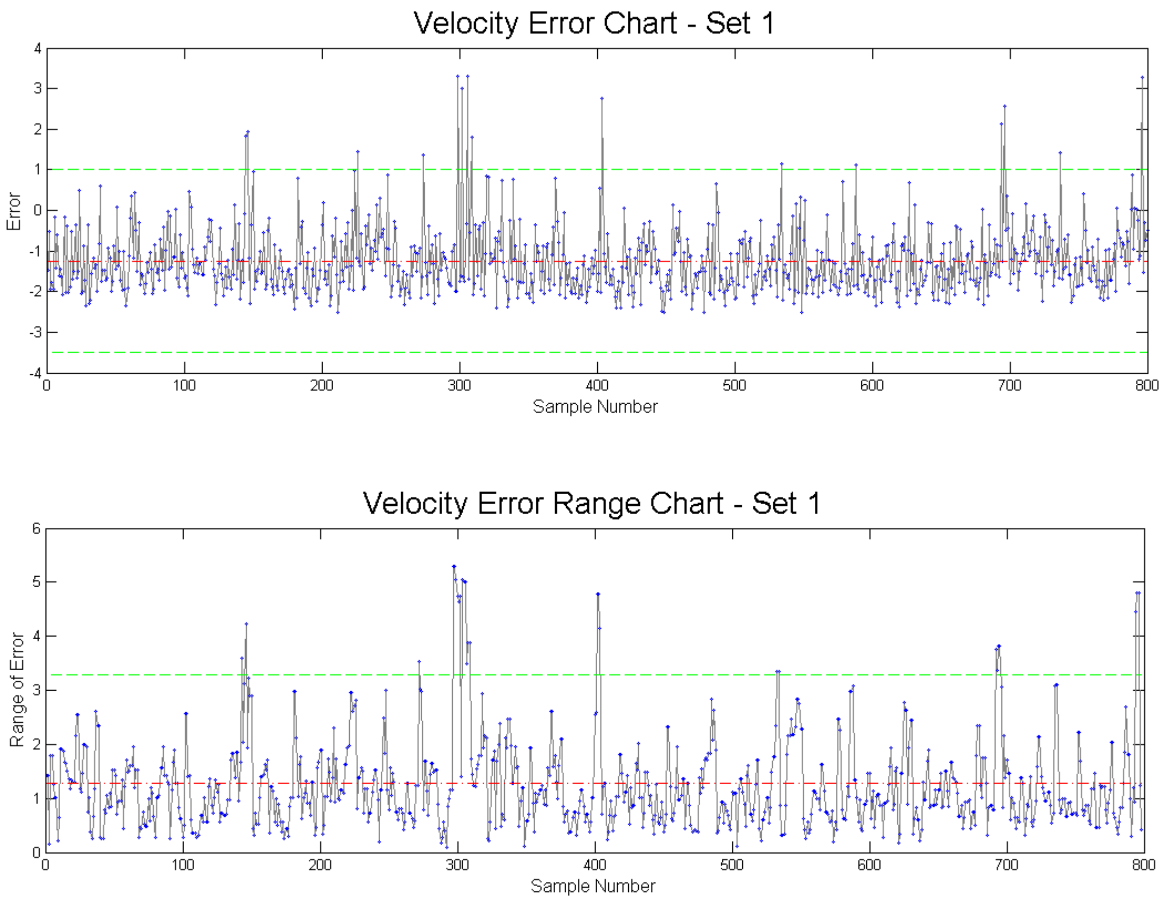

Figure A.1. Raft Testing Control Chart - Set 1

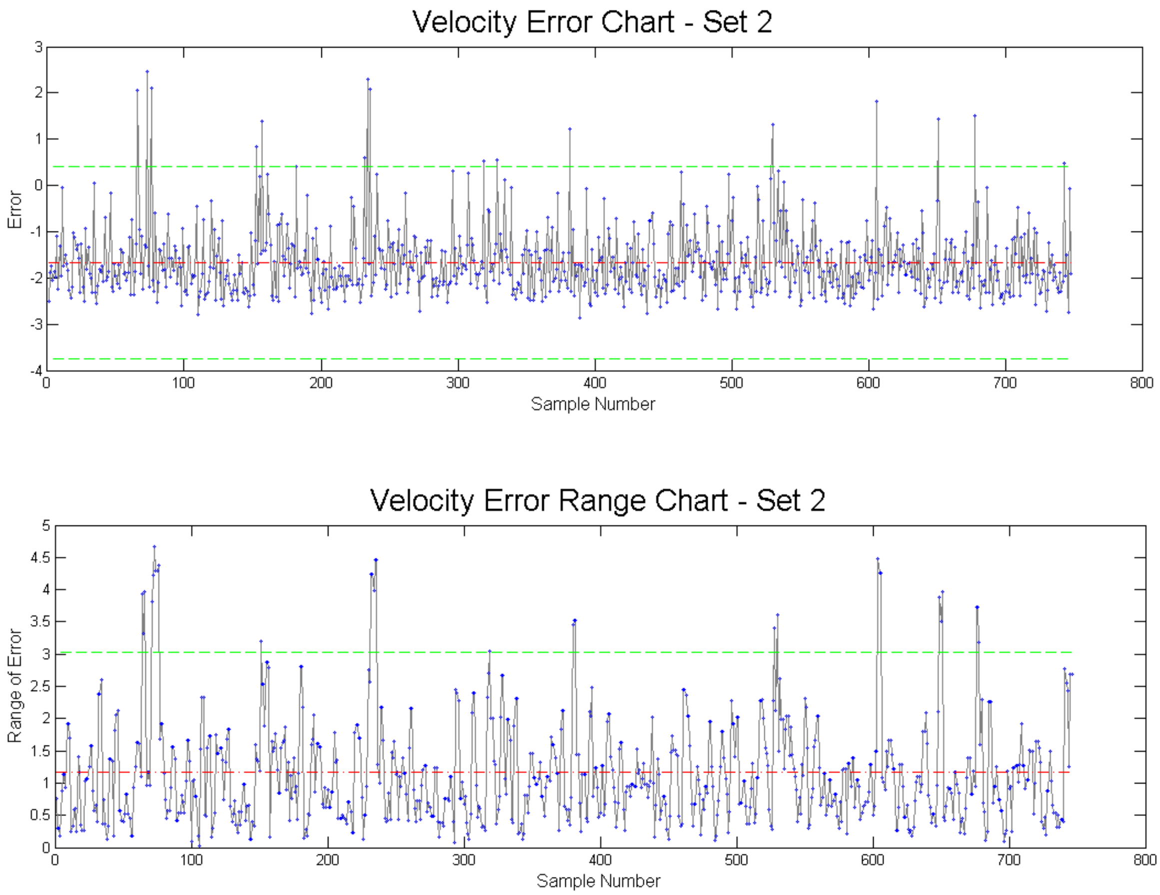

Figure A.2. Raft Testing Control Chart - Set 2

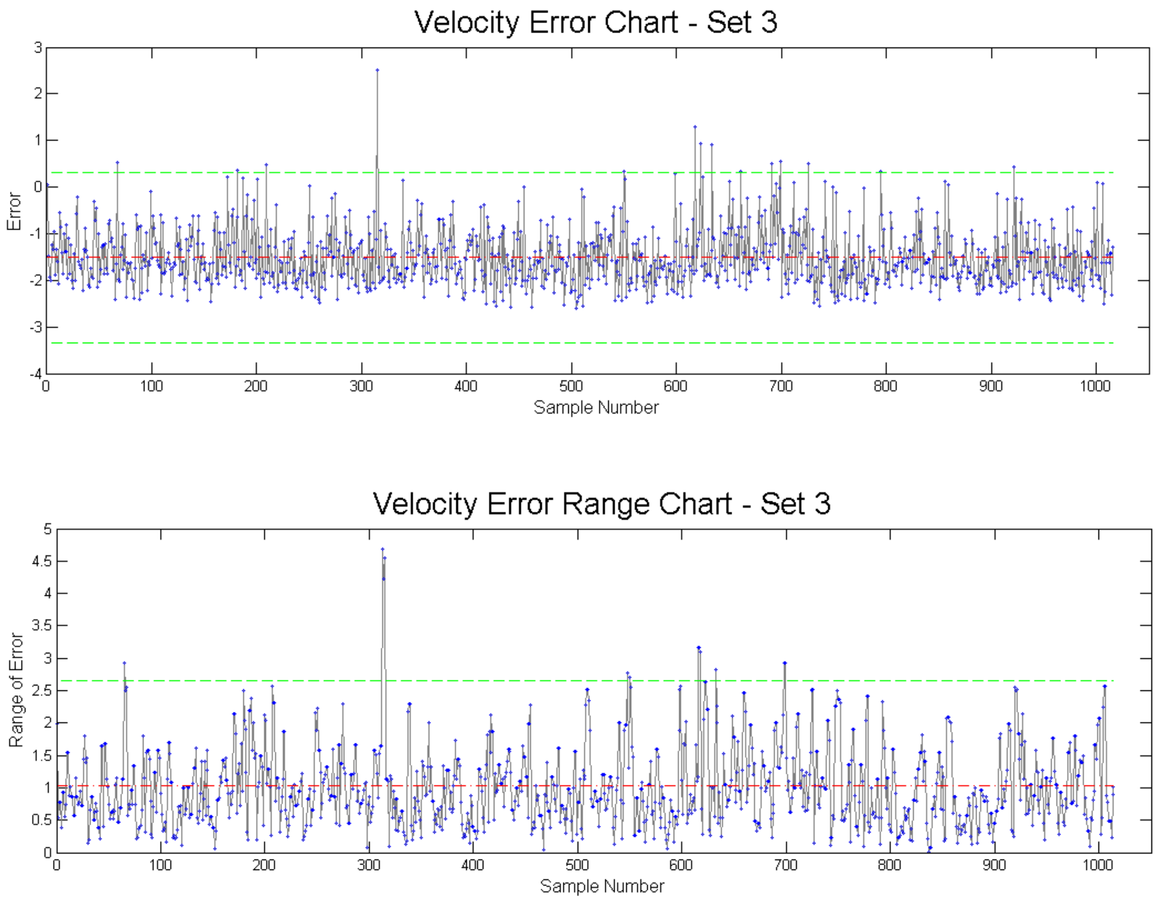

Figure A.3. Raft Testing Control Chart - Set 3

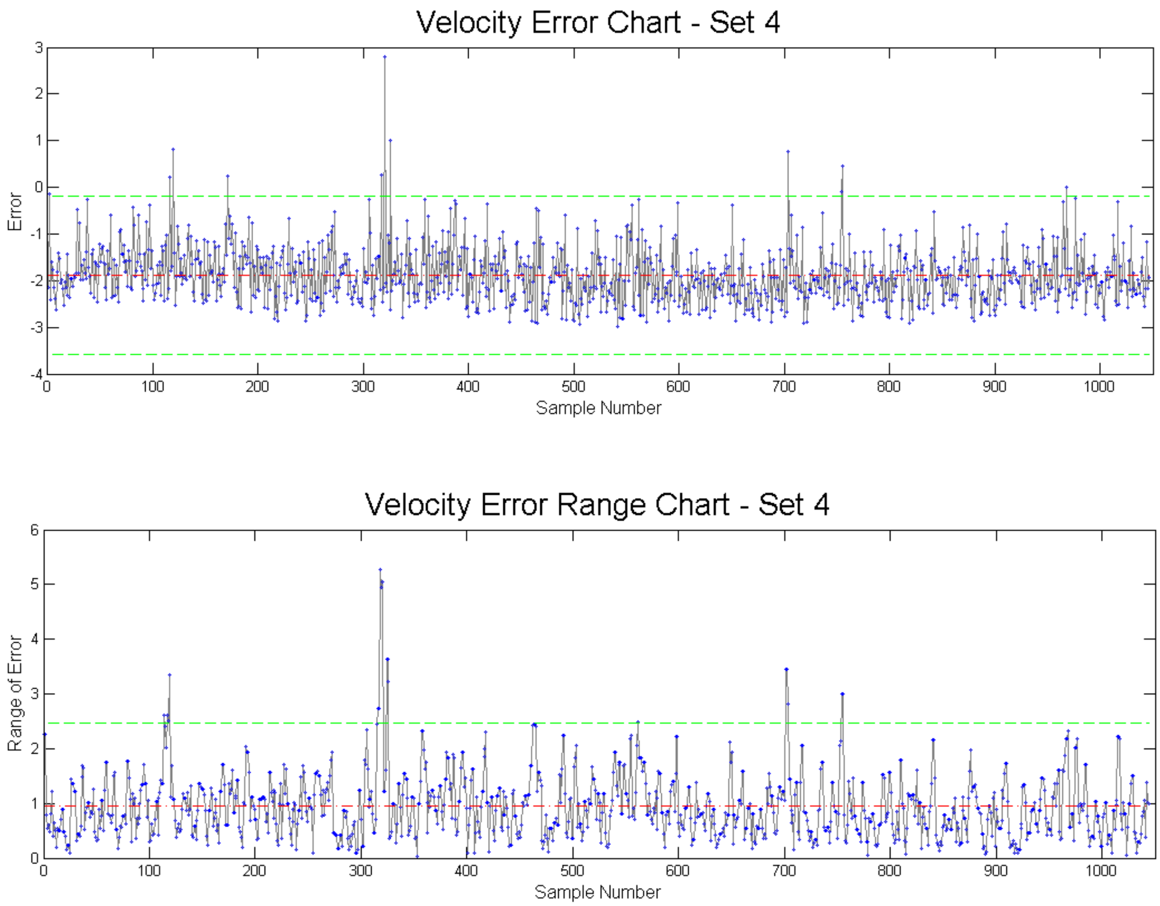

Figure A.4. Raft Testing Control Chart - Set 4

B. THIN FILM INSTABILITY APPENDICIES

B.1 Full Image Processing Code with Supporting Functions

```
%% Code Header

% filename: EvapCodeTest.m
% author: Eric W. Kalenauskas
% date created: 4/7/09
% last modified: 5/26/09

% Code Summary:
%This code is designed to extract the critical wavenumber from a sequence
% of schlieren images.

%This code employes user created functions to load images,
% implement Sequence Principle Component Analysis (SPCA), further process
% the resulting component images, perform transform to frequency space and
% implement an energy filter on the resulting point cloud.  The code will
% then use 2-D PCA to collapse the data on the first principle component
% direction and determine frequencies of high signal density to extract the
% critical wave number from the image.

% This code is the first adaptation of previous investigative work to
% handle full sequences of images.

%% Start Code

% clear workspace, command window, and close figures
clear, clc, close all

% set code start time
tic

%% Load Files

% create structure of image file names
files = dir('*.JPG');

% determine number of images loaded
f_length = length(files);

% determine image size
imsize = size(imread(files(1).name));

% load images to matrix
```

```
numload = 0;
Img = zeros(imsize(1),imsize(2),f_length,'uint8');
display('Loading Images...')
for i = 1:f_length
    Img(:,:,i) = imread(files(i).name);
    numload = numload + 1;
    display(num2str(numload))
end
display('...Image Loading Complete')
clear numload imsize files f_length i

%% Image Sequence Principle Component Analysis
Img = SPCA(Img,6,3);

%% Pre FFT Processing
Img = PreFFTProcessing(Img);

%% 2D FFT
%Img = ImgFFT(Img,2,0.70);

%% Point Cloud PCA & Frequency Identification
% will be adapted to sequence work from older code ... in progress
% display('Running Point cloud PCA & Frequency Identifaction...')
% freq_dist = PointCloudPCA(Img);
% display('... Frequencies Extracted')
%% Outputs
% will be adapted to sequence work from older code

display('***Master Code Complete***')
toc
```

```
function [Img_SPCA] = SPCA(Img,seq_length,PC_num)

imsize = size(Img);

% build images into SPCA data matrix
SPCA_data_in = zeros((imsize(1)*imsize(2)),imsize(3));
display('Building Sequence PCA Data Matix...')
for k = 1:imsize(3)
    I = double(Img(:,:,k));
    a = 1;
    b = imsize(1);
    for j = 1:imsize(2)
        Iv(a:b) = I(:,j);
        a = a + imsize(1);
        b = b + imsize(1);
    end
    SPCA_data_in(:,k) = Iv;
    clear a b Iv I
end
```

```
display('...Complete')

% preallocate SPCA_data_out
SPCA_data_out = zeros((imsize(1)*imsize(2)),imsize(3));

display('SPCA Running...')
% SPCA loop
for a = 1:(imsize(3) - seq_length)
    SPCA_short_in = SPCA_data_in(:,a:(a+(seq_length-1)));
    for b = 1:seq_length
        SPCA_short_in(:,b) = SPCA_short_in(:,b) - mean(SPCA_short_in(:,b));
    end
    SPCA_cov = cov(SPCA_short_in);
    [SPCA_evect,SPCA_eval] = eig(SPCA_cov);
    SPCA_comp_vect = (SPCA_evect(:,seq_length-PC_num+1))';
    SPCA_short_out = SPCA_comp_vect' * (SPCA_comp_vect * SPCA_short_in');
    for b = 1:seq_length
        SPCA_short_out(:,b) = SPCA_short_out(:,b) + mean(SPCA_short_in(:,b));
    end
    SPCA_data_out(:,a) = SPCA_short_out(1,:);
end
display('...SPCA Complete')

display('Extracting Images...')
% extract images from SPCA data matrix
Img_SPCA = zeros(imsize(1),imsize(2),imsize(3));
for k = 1:imsize(3)
    a = 1;
    b = imsize(1);
    for j = 1:imsize(2)
        Img_SPCA(:,j,k) = SPCA_data_out(a:b,k);
        a = a + imsize(1);
        b = b + imsize(1);
    end
end
Img_SPCA = uint8(Img_SPCA);
Img_SPCA = Img_SPCA(:,:,1:imsize(3)-seq_length);
display('...Images Extracted')
```

```
function [Img] = PreFFTProcessing(Img)

display('Running Pre FFT Image Processing...')
imsize = size(Img);

for k = 1:imsize(3)
    I = Img(:,:,k);
    I = imadjust(I,[0 1],[0.5 1]);
```

```
    J(:,:,k) = I;
end

for k = 1:imsize(3)
    I = J(:,:,k);
    I = im2bw(I,0.54);
    Img(:,:,k) = I;
end

Img = logical(Img);
display('...Pre FFT Image Processing Complete')
```

```
function [FFTPointCloud] = ImgFFT(Img,HPfiltsize,PME)

display('Running ImgFFT...')
imsize = size(Img);
height = imsize(1);
width = imsize(2);

for a = 1:imsize(3)

    J = fftshift(fft2(Img(:,:,a)));

    ycenter = height / 2;
    xcenter = width / 2;
    filtsize = HPfiltsize;

    for i = 1:height
        for j = 1:width
            if sqrt((abs(i - ycenter)^2) + (abs(j - xcenter)^2)) ≤
                filtsize
                J(i,j) = 0;
            end
        end
    end

    A = log(abs(J));
    maxfreq = max(max(A));
    freqlog = zeros(imsize(1),imsize(2));
    k = 1;

    for i = 1:height
        for j = 1:width
            if A(i,j) ≥ (maxfreq * PME) % <-- Percent Max Energy
                freqlog(i,j) = 1;
            end
        end
    end

    FFTPointCloud(:,:,a) = freqlog(:,:);
```

```
end
display('...ImgFFT Complete')


function [frequency_log] = PointCloudPCA(Img)

imsize = size(Img);

for c = 1:imsize(3)

    % clear matrix A for reuse
    clear A B xmean ymean orig_data

    % redefine point cloud image and extract size info
    I = Img(:,:,c);
    I = im2bw(I);
    I_size = size(I);

    % determine X and Y coordinates of point cloud and build PCA data
        matrix
    k = 1;
    for i = 1:I_size(1)
        for j = 1:I_size(2)
            if I(i,j) == 1
                Ax(k) = j;
                Ay(k) = i;
                k = k+1;
            end
        end
    end

    A(:,1) = Ax;
    A(:,2) = Ay;


    % center point cloud about (0,0)
    xmean = mean(A(:,1));
    ymean = mean(A(:,2));

    B(:,1) = A(:,1) - xmean;
    B(:,2) = A(:,2) - ymean;

    % calculate covariance matrix
    Cov_matrix = cov(B);

    % calculate eigenvectors and eigenvalues
    [E_vect,E_val] = eig(Cov_matrix);

    maxeval = 0;
    maxevectnum = 0;
```

```
for i = 1:length(E_val)
    j = E_val(:,i);
    if max(j) > maxeval
        maxeval = max(j);
        maxevectnum = i;
    end
end

E_vect_max = E_vect(:,maxevectnum);

% build feature vector with 1st principle component
feature_vect = [E_vect_max];
feature_vect = feature_vect';
B = B';

% calculate transformed matrix
final_data = feature_vect * B;

% convert back to XY space
orig_data = (feature_vect' * final_data);

% uncenter data
%orig_data(1,:) = orig_data(1,:) + xmean;
%orig_data(2,:) = orig_data(2,:) + ymean;

orig_data = orig_data';

% calculate distance of each data point along 1st principle
   component
freq_dist = sqrt((orig_data(:,1).^2) + (orig_data(:,2).^2));

%%
% clear variable A for reuse
clear A

% redefine 1st PC point cloud
A = freq_dist;

% set range for density criteria
D_width = 0.5;

% count points occuring at each freq
data_size = length(A);

for i = 1:data_size
    D(i) = 0;
    for j = 1:data_size
        if (i - D_width) < A(j) && A(j) < (i + D_width)
            D(i) = D(i) + 1;
        end
    end
```

```
    end

    % find limits of the data
    j = 1;
    for i = 1:data_size
        if D(i) ≠ 0
            mark(j) = i;
            j = j + 1;
        end
    end

    % limit range to data limits
    D = D(min(mark):max(mark));
    data_size = length(D);
    maxval = max(D);

    % find the highest occuring frequency
    for i = 1:data_size
        if D(i) == maxval
            freq = i;
        end
    end

    % determine max freq distance from data center (0 Hz)
    %freq = abs(freq - (data_size/2))


    frequency_log(c) = freq;


end
```

BIBLIOGRAPHY

[1] S. Chandrasekhar. *Hydrodynamic and Hydromagnetic Stability*. Dover, 1961.

[2] S. H. Davis, S. G. Bankoff, and J. P. Burelbach. Steady thermo capillary flows of thin liquid layers. ii. experiment. *Phys. Fluids*, 1990.

[3] R. E. DeVor, T. Chang, and J. W. Sutherland. *Statistical Quality Design and Control - Contemporary Concepts and Methods*. Pearson Prentice Hall, 2007.

[4] J Eul, A Kastamo, O Kingstedt, P Kurtz, and E St.Ours. Test-bench assessment of the uncertainty of radial velocities for an acoustic doppler current profiler. Technical report, Capstone Design, Dept. of Mechanical Engineering - Engineering Mechanics, College of Engineering, Michigan Technological University, 2008.

[5] D.W. Holder and R.J. North. *Schlieren Methods*. National Physical Laboritory, 1963.

[6] J. Holman. *Experimental Methods for Engineers*. McGraw-Hill, 2001.

[7] J.T. Kimball, J.C. Hermanson, and J.S. Allen. Convective structure and heat transfer in thin, evaporating films. In *The 20th International Symposium on Transport Phenomena*, 2009.

[8] Pijush K. Kundu. *Fluid Mechanics*. Academic Press, 1990.

[9] D. S. Mueller, J. D. Abad, C. M. Garcia, J. W. Gartner, M. H. Garcia, and K. A. Oberg. Errors in acoustic doppler current profiler vewlocity measurements caused by flow distrubance. *Journal of Hydraulic Engineering*, December:1411–1420, 2001.

[10] K. Oberg. In search of easy-to-use methods for calibrating adcp's for velocity and discharge measurements. Technical report, US Geological Survey, Office of Surface Water, 2002.

[11] A. Oron, S. Davis, and S. G. Bankoff. Long-scale evolution of thin liquid films. *Reviews of Modern Physics*, 69:931–980, 1997.

[12] Swapnil A. Padate. Dynamics of evaporating films: A numerical model and an experimental approach. Master's thesis, Michigan Technological University, 2006.

[13] Jonathon Shlens. A tutorial on principle component analysis. Technical report, Systems Neurobiology Laboratory, Salk Institute for Biological Studies and Institute for Nonlinear Science, University of California, San Diego, 2005.